expressing HA-associated signals easily, but cells expressing Myc-associated signals were sparse (Fig. 5a). Most of the HA- and Myc-associated signals were segregated subcellularly, with those of HA-tagged hERG(WT) at the periphery of cells, whereas those of Myc-tagged hERG(ΔAT) remained intracellularly (Fig. 5b, c, d). These results suggest that the Myc-tagged hERG(ΔAT) subunit was expressed at lower levels compared with the HA-tagged hERG(WT) subunit and that what little mutant protein was produced remained localized within the cells.

Electrophysiological analysis of the hERG(ΔAT) subunit

To examine whether the hERG(ΔAT) subunit can form functional channels in the absence or presence of the hERG(WT) subunit, we compared whole cell currents from HEK-293 T cells transfected with hERG(ΔAT) cDNA, both with and without hERG(WT) cDNA. The transfected cells were stimulated using a double-step voltage protocol (Fig. 6a, schematic). In the first step (i.e., at a relatively high voltage), the hERG channel underwent activation as well as inactivation. During the second step (i.e., at a less positive voltage), the hERG channel was relieved from inactivation and produced a large "tail" current (Fig. 6a, hERG(WT) traces). The tail current measured under these conditions included virtually no component mediated by the HEK-293 T cell's native voltage-dependent current [18] because its amplitude did not differ notably between cells transfected with *hERG*(WT) cDNA and those transfected with *GFP* cDNA alone (Fig. 6b).

We presume that *hERG*(WT)-transfected cells displayed hERG channel-mediated tail current, given that its peak density at a first-step voltage of 60 mV (49.1±5.4 pA/pF [mean± SEM, n=18]) was significantly (P<0.001, rank-sum test) larger than that of *GFP*-transfected cells (3.0±0.6 pA/pF; n=12; Fig. 6b). By contrast, the *hERG*(ΔAT)-transfected cells did not display similar hERG channel-mediated tail currents because their peak density (3.7±0.6 pA/pF; n=14) did not differ from that of the *GFP*-transfected cells (Fig. 6b). In addition, the peak density of the tail current of the *hERG*(ΔAT)-transfected cells was significantly (P<0.001, rank-sum test) smaller than that of the *hERG*(WT)-transfected cells. These results suggest that the hERG(ΔAT) subunits cannot form functional channels on their own.

The amplitude of the tail current produced by the HEK-293 T cells transfected with a 1:1 mixture of *hERG*(ΔAT) and *hERG*(WT) cDNAs (peak current density at a first-step voltage of 60 mV, 50.4±7.9 pA/pF; n=14; Fig. 6b) was comparable to that of the *hERG*(WT)-transfected cells. One possibility suggested by this result is that hERG(ΔAT) subunits might form functional channels with the aid of hERG(WT) subunits. Alternatively, homomeric hERG(WT) channels might account for a predominant portion of the tail current, with the hERG(ΔAT) subunit-containing channels making only slight or no contribution to the tail current. To assess these possibilities, we measured the tail current in cells transfected with a 30:1 mixture of *hERG*(ΔAT) and *hERG*(WT) cDNAs, in which the mutant subunits outnumbered the wild-type subunits. In this case, the peak current density (24.9±6.9 pA/pF, n=10) was significantly (P<0.001, rank-sum test) less than that of cells transfected with *hERG*(WT) only (Fig. 6b).

To quantify the voltage dependence of the activation extent, the Boltzmann equation was fitted to the plot of the normalized peak tail current amplitude against first-step voltage (Fig. 6c). The half-maximal activation voltage (V_{half}) and slope (K) of the cells transfected with the 30:1 mutant/WT mixture (−3.28±3.53 mV and 8.99±1.19, respectively; n=10) were not significantly different from those of *hERG*(WT)-transfected cells (−0.30±1.59 mV and 8.18±0.79, respectively; n=18). In addition, the activation time-course depicted by plotting the peak tail current amplitude against the varied duration of the first-step voltage did not differ notably between the *hERG*(WT)-transfected cells (time constant 125.0±14.1 ms; n=17) and the 30:1-transfected cells (121.7±15.5 ms; n=10; Fig. 6d). These results suggest that the hERG(ΔAT) subunit does not influence the kinetic properties of the hERG(WT) channels.

Discussion

Since many arrhythmia patients present genetic anomalies, cases of sudden unexpected deaths can be expected where there are family histories of arrhythmias. Thus, molecular biological analyses would be useful for exploring the cause of such cases. Of course, careful ethics considerations are essential. Our examination of the present case demonstrated that the patient's cause of death was ventricular arrhythmia due to an unreported ion channel disorder. Such analyses would be useful for not only exploring the cause of death, but also in contributing to clinical and basic research on arrhythmia.

This study investigated the molecular and electrophysiological properties of the product of a novel ΔAT mutant *hERG* we identified from a patient who died from SCD. This mutation leads to the frameshift M579fs+75X and the production of a truncated hERG subunit that lacks the C-terminus. Although the patient was heterozygous for the ΔAT mutation, she displayed mild symptoms of QTc prolongation on ECG, dilatation of the left ventricle at autopsy, and histologically apparent interstitial fibrosis of the left ventricle and atrioventricular conduction system.

More than 30 % of known *hERG* mutations are of the nonsense or frameshift type that introduce premature termination codons [19, 20]. mRNAs containing a premature termination codon more than 50–55 nucleotides upstream

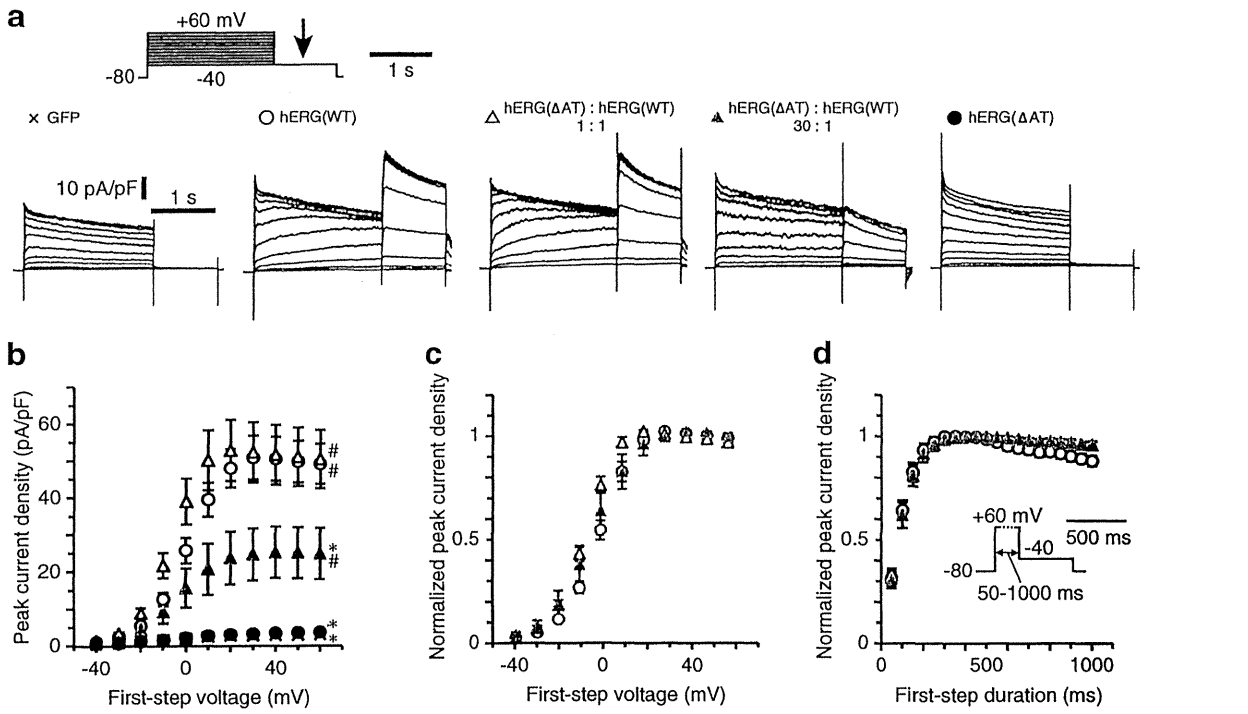

Fig. 6 Whole cell currents in HEK-293 T cells transfected with *hERG*(WT) and/or *hERG*(ΔAT). **a** Sample current responses of HEK-293 T cells transfected with the indicated genes. Currents mediated by hERG channels became evident as "tail" currents during the second step of the voltage stimulus protocol (*arrow* in schematic); n=18, 14, 14, 10, and 12 for cells transfected with *hERG*(WT), *hERG*(ΔAT), 1:1 and 30:1 mixtures of these genes, and the *GFP* gene alone (control), respectively. **b** Mean peak density of the tail current as a function of the first-step voltages. #P<0.001 (rank-sum test) compared with *GFP*-transfected cells; *P<0.001 (rank-sum test) compared with *hERG*(WT)-transfected cells. **c** Relative peak amplitude of the tail current as a function of the first-step voltage. **d** Activation time-course of hERG channels. Mean relative peak amplitude of the tail current elicited by a double-voltage step stimulus plotted as a function of the duration of the first-step voltage. In this experiment, the duration was varied as shown schematically in the *inset*

of the last exon–exon junction often undergo nonsense-mediated mRNA decay, which effectively reduces the amount of abnormal mRNAs [21]. We found that the level of transcripts from the *hERG*(ΔAT) allele was much lower than that for the *hERG*(WT) allele. One possibility suggested from this result is that *hERG*(ΔAT) mRNA might be degraded via the nonsense-mediated decay pathway.

The immunoblot analysis using HEK-293 T cells showed that hERG(ΔAT) produced lower protein levels than hERG(WT), regardless of whether the cells were co-transfected with hERG(WT) cDNA (Fig. 4). Confocal microscopy confirmed that the expression level of the hERG(ΔAT) subunit was much lower than that of the hERG(WT) subunit and showed that the slight amounts of mutant protein produced remained localized within the cells. One possibility arising from these results is that the reduced surface expression of the hERG(ΔAT) subunit simply reflects decreased protein production. Another possibility is that trafficking of hERG(ΔAT) is impaired, leading to decreased surface expression. Truncated proteins are often trafficking deficient, misfolded, misrouted, and consequently subjected to endoplasmic reticulum-associated degradation [22]. Therefore, both production and trafficking of the hERG(ΔAT) subunit may be impaired, but further study is required to gauge the relative influence of these two mechanisms.

Nonsense or frameshift mutations are located more frequently in the C-terminal region of hERG channel subunits than in the transmembrane pore domain (S5–loop–S6) [8]. The frameshift mutation we evaluated here is located in the S5-pore. Immunoblotting or immunohistochemistry experiments have confirmed that the Q725X [17] frameshift mutation in the C-terminus disrupts the tetrameric assembly of hERG and that E698X [23] and R863X [23, 24] lead to defective protein trafficking. Moreover, patch-clamp experiments have confirmed that these mutant proteins fail to produce functional homomeric channels and exert at most only a weak dominant-negative effect on WT proteins. Minigene-based experiments have demonstrated that hERG mutations such as P926Afs+14X [25], R1014X [26], R1005fs+50X, and Q1070X [27], all lead to degradation of the mutant mRNAs via the nonsense-mediated decay pathway. The functional consequence of the ΔAT frameshift mutation is therefore likely to be due to loss of functional hERG channels on the plasma membrane through multiple cellular mechanisms.

hERG(ΔAT)-transfected HEK-293 T cells were observed to lack a tail current, suggesting that hERG(ΔAT) subunits cannot form functional channels on their own. In contrast, cells co-transfected with *hERG*(ΔAT) and *hERG*(WT) did display a tail current. We surmise that this current is mediated largely by homomeric hERG(WT) channels, for the following reasons: First, the current amplitude decreased with the amount of *hERG*(WT) used in the transfection (Fig. 6b). Second, the cells transfected with a 30:1 mixture of *hERG*(ΔAT)/*hERG*(WT) displayed a tail current with voltage and time dependencies of activation similar to those of cells transfected with *hERG*(WT) only. The simplest interpretation of these findings is that the hERG(ΔAT) subunit contributes little to functional channel formation even in the presence of the hERG(WT) subunit. We cannot exclude the possibility that hERG(ΔAT) and hERG(WT) subunits associate to form functional heteromeric channels with small conductances. However, such heteromeric channels would most likely comprise only a small fraction of the total hERG channel population because hERG(WT) subunits appeared to greatly outnumber hERG(ΔAT) subunits on the cell surface (Fig. 5). Therefore, heteromeric channels would contribute little to whole cell electrical activity. This scenario may explain the mild cardiac symptoms of our patient, who was heterozygous for *hERG*(ΔAT). Furthermore, a homozygous *hERG*(ΔAT) carrier would most likely display severe symptoms resulting from a lack of functional hERG channels (Fig. 6a, b).

Our patient with the *hERG*(ΔAT) mutation displayed only mild symptoms during her everyday life and was categorized into an intermediate risk group in terms of her QTc interval, genotype, and gender. Nevertheless, she died from SCD 10 h after awakening from general anesthesia; her postoperative course was uneventful otherwise. The loss-of-function mutation in *hERG* identified in the current study might underlie the pathogenesis of her SCD. Patients with LQT2 are highly vulnerable to alterations in their physical and mental states that involve sympathetic surges [6]. For example, emotional stress, exercise, and various drugs [28] may trigger life-threatening arrhythmias in these patients. Our findings provide deeper insight into the genotype–phenotype relationship underlying LQT2 and a better understanding of the variability of the clinical presentation and subsequent risk stratification of LQTS in general.

Conclusion

We identified a novel *hERG* frameshift mutation (*hERG*(ΔAT)) in a patient who died from SCD. The ΔAT mutation decreased the number of functional hERG channels presumably by impairing the posttranscriptional and post-translational processing of the *hERG*(ΔAT) product. This decrease may explain, at least in part, the mild cardiac symptoms of our patient (who was heterozygous for *hERG*(ΔAT)) in everyday life and may have later contributed to her death.

Acknowledgments We thank Drs. Kenshi Hayashi (Kanazawa University Graduate School of Medical Science, Kanazawa, Japan), Sabina Kupershmidt (Vanderbilt University School of Medicine, Nashville, USA), and Jun-ichi Miyazaki (Osaka University Medical School, Osaka, Japan) for providing plasmids. We also thank Prof. K. Fukurotani for the opportunity to perform this work. This work was supported in part by KAKENHI grants from MEXT, Japan, to T.T. (19045019, 20022025, 20500284, 21026011, and 23500384) and a KAKENHI grant from JSPS, Japan, to Y.H. (24590852).

Conflict of interest The authors declare that they have no conflict of interest.

Ethics statement The experiments described in this manuscript conform to the Declaration of Helsinki, and the protocols of gene sampling and manipulation were approved by the University of Toyama's committee on the usage of human genetic material (#24-1).

References

1. Splawski I, Shen J, Timothy KW, Lehmann MH, Priori S, Robinson JL, Moss AJ, Schwartz PJ, Towbin JA, Vincent GM, Keating MT (2000) Spectrum of mutation in long-QT syndrome genes: KVLQT1, HERG, SCN5A, KCNE1, and KCNE2. Circulation 102:1178–1185
2. Splawski I, Timothy KW, Sharpe LM, Decher N, Kumar P, Bloise R, Napolitano C, Schwartz PJ, Joseph RM, Condouris K, Tager-Flusberg H, Priori SG, Sanguinetti MC, Keating MT (2004) Cav1.2 calcium channel dysfunction causes a multisystem disorder including arrhythmia and autism. Cell 119:19–31
3. Vincent GM, Timothy KW, Leppert M, Keating M (1992) The spectrum of symptoms and QT intervals in carriers of the gene for the long-QT syndrome. N Engl J Med 327:846–852
4. Hedley PL, Jørgensen P, Schlamowitz S, Wangari R, Moolman-Smook J, Brink PA, Kanters JK, Corfield VA, Christiansen M (2009) The genetic basis of long QT and short QT syndromes: a mutation update. Hum Mutat 30:1486–1511
5. Yang Y, Yang Y, Liang B, Liu J, Li J, Grunnet M, Olesen SP, Rasmussen HB, Ellinor PT, Gao L, Lin X, Li L, Wang L, Xiao J, Liu Y, Liu Y, Zhang S, Liang D, Peng L, Jespersen T, Chen YH (2010) Identification of a Kir3.4 mutation in congenital long QT syndrome. Am J Hum Genet 86:872–880
6. Cerrone M, Priori SG (2011) Genetics of sudden death: focus on inherited channelopathies. Eur Heart J 32:2109–2118
7. Perrin MJ, Subbiah RN, Vandenberg JI, Hill AP (2008) Human ether-a-go-go related gene (hERG) K+channels: function and dysfunction. Prog Biophys Mol Biol 98:137–148
8. Shimizu W, Moss AJ, Wilde AA, Towbin JA, Ackerman MJ, January CT, Tester DJ, Zareba W, Robinson JL, Qi M, Vincent GM, Kaufman ES, Hofman N, Noda T, Kamakura S, Miyamoto Y, Shah S, Amin V, Goldenberg I, Andrews ML, McNitt S (2009) Genotype–phenotype aspects of type 2 long QT syndrome. J Am Coll Cardiol 54:2052–2062
9. Nishida N, Ikeda N, Kudo K, Tsuji A, Kiyoshima A (2002) Forensic significance of conduction system abnormalities as a precise cause of accidental death. Int J Legal Med 116:344–349

10. Harvey PA, Leinwand LA (2011) The cell biology of disease: cellular mechanisms of cardiomyopathy. J Cell Biol 194:355–365
11. Hata Y, Kominato Y, Takizawa H (2007) Identification and characterization of a novel antisense RNA transcribed from the opposite strand of the human blood group ABO gene. Transfusion 47:842–851
12. Snyders DJ, Chaudhary A (1996) High-affinity open channel block by dofetilide of HERG expressed in a human cell line. Mol Pharmacol 49:949–955
13. Niwa H, Yamamura K, Miyazaki J (1991) Efficient selection for high-expression transfectants with a novel eukaryotic vector. Gene 108:193–199
14. Ho SN, Hunt HD, Horton RM, Pullen JK, Pease LR (1898) Site-directed mutagenesis by overlap extension using the polymerase chain reaction. Gene 77:51–59
15. Ochman H, Gerber AS, Hartl DL (1988) Genetic applications of an inverse polymerase chain reaction. Genetics 120:621–623
16. Barahona-Dussault C, Benito B, Campuzano O, Iglesias A, Leung TL, Robb L, Talajic M, Brugada R (2010) Role of genetic testing in arrhythmogenic right ventricular cardiomyopathy/dysplasia. Clin Genet 77:37–48
17. Gong Q, Keeney DR, Robinson JC, Zhou Z (2004) Defective assembly and trafficking of mutant HERG channels with C-terminal truncations in long QT syndrome. J Mol Cell Cardiol 37:1225–1233
18. Kinoshita K, Yamaguchi Y, Nishide K, Kimoto K, Nonobe Y, Fujita A, Asano K, Tabata T, Mori H, Inoue H, Hata Y, Fukurotani K, Nishida N (2012) A novel missense mutation causing a G487R substitution in the S2–S3 loop of human ether-à-go-go-related gene channel. J Cardiovasc Electrophysiol 23:1246–1253
19. Tester DJ, Will ML, Haglund CM, Ackerman MJ (2005) Compendium of cardiac channel mutation in 541 consecutive unrelated patients referred for long QT syndrome genetic testing. Heart Rhythm 2:507–517
20. Millat G, Chevalier P, Restier-Miron L, Da Costa A, Bouvagnet P, Kugener B, Fayol L, Gonzàlez Armengod C, Oddou B, Chanavat V, Froidefond E, Perraudin R, Rousson R, Rodriguez-Lafrasse C (2006) Spectrum of pathogenic mutations and associated polymorphisms in a cohort of 44 unrelated patients with long QT syndrome. Clin Genet 70:214–227
21. Nagy E, Maquat LE (1998) A rule for termination-codon position within intron-containing genes: when nonsense affects RNA abundance. Trends Biochem Sci 23:198–199
22. Stephenson LS, Maquat LE (1996) Cytoplasmic mRNA for human triosephosphate isomerase is immune to nonsense-mediated decay despite forming polysomes. Biochimie 78:1043–1047
23. Yan Y, Teng S, Li N, Zhang Y, Boyden PA, Pu J (2009) Aminoglycoside antibiotics restore functional expression of truncated HERG channels produced by nonsense mutations. Hear Rhythm 6:553–560
24. Teng S, Ma L, Dong Y, Lin C, Ye J, Bähring R, Vardanyan V, Yang Y, Lin Z, Pongs O, Hui R (2004) Clinical and electrophysiological characterization of a novel mutation R863X in HERG C-terminus associated with long QT syndrome. J Mol Med 82:189–196
25. Zarraga IG, Zhang L, Stump MR, Gong Q, Vincent GM, Zhou Z (2011) Nonsense-mediated mRNA decay caused by a frameshift mutation in a large kindred of type 2 long QT syndrome. Hear Rhythm 8:1200–1206
26. Gong Q, Zhang L, Vincent M, Horne BD, Zhou Z (2007) Nonsense mutations in hERG cause a decrease in mutant mRNA transcripts by nonsense-mediated mRNA decay in human long-QT syndrome. Circulation 116:17–24
27. Gong Q, Stump MR, Zhou Z (2011) Inhibition of nonsense-mediated mRNA decay by antisense morpholino oligonucleotides restores functional expression of hERG nonsense and frameshift mutations in long-QT syndrome. J Mol Cell Cardiol 50:223–229
28. Sanguinetti MC, Tristani-Firouzi M (2006) hERG potassium channels and cardiac arrhythmia. Nature 440:463–469

SCIENTIFIC REPORTS

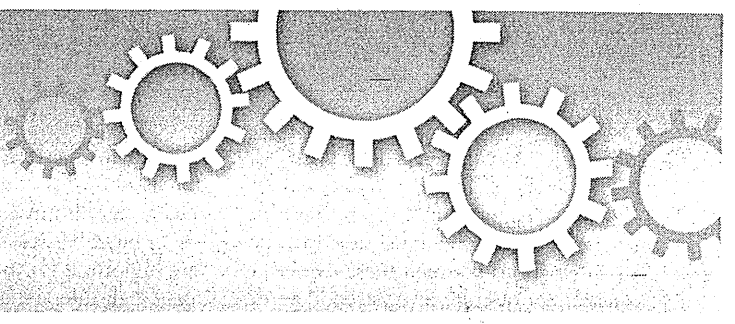

OPEN

SUBJECT AREAS:
ACUTE INFLAMMATION
EXPERIMENTAL MODELS OF DISEASE
MIRNAS
EXTRACELLULAR SIGNALLING MOLECULES

Received
28 September 2014

Accepted
22 January 2015

Published
17 February 2015

Correspondence and requests for materials should be addressed to S.Y. (seiyama@med.u-toyama.ac.jp)

* These authors contributed equally to this work.

Inflammation-induced endothelial cell-derived extracellular vesicles modulate the cellular status of pericytes

Seiji Yamamoto[1]*, Shumpei Niida[2]*, Erika Azuma[1,3], Tsutomu Yanagibashi[4,7], Masashi Muramatsu[2,5], Ting Ting Huang[1], Hiroshi Sagara[6], Sayuri Higaki[2], Masashi Ikutani[7], Yoshinori Nagai[7], Kiyoshi Takatsu[4,7], Kenji Miyazaki[8], Takeru Hamashima[1], Hisashi Mori[9], Naoyuki Matsuda[10], Yoko Ishii[1] & Masakiyo Sasahara[1]

[1]Department of Pathology, Graduate School of Medicine and Pharmaceutical Sciences, University of Toyama, Toyama, Japan, [2]Bio Bank Omics Unit, National Center for Geriatrics and Gerontology, Aichi, Japan, [3]Manufacturing & Engineering Lab., Astellas Pharma Inc., Tsukuba, Japan, [4]Toyama Prefectural Institute for Pharmaceutical Research, Toyama, Japan, [5]Department of Cancer Genetics, Roswell Park Cancer Institute, Buffalo, NY, USA, [6]Medical Proteomics Laboratory, Institute of Medical Science, The University of Tokyo, Tokyo, Japan, [7]Department of Immunobiology and Pharmacological Genetics, Graduate School of Medicine and Pharmaceutical Sciences, University of Toyama, Toyama, Japan, [8]The Center for Graduate Medical Education, Jichi Medical University, Tochigi, Japan, [9]Department of Molecular Neuroscience, Graduate School of Medicine and Pharmaceutical Sciences, University of Toyama, Toyama, Japan, [10]Department of Emergency and Critical Care Medicine, Nagoya University, Nagoya, Japan.

Emerging lines of evidence have shown that extracellular vesicles (EVs) mediate cell-to-cell communication by exporting encapsulated materials, such as microRNAs (miRNAs), to target cells. Endothelial cell-derived EVs (E-EVs) are upregulated in circulating blood in different pathological conditions; however, the characteristics and the role of these E-EVs are not yet well understood. *In vitro* studies were conducted to determine the role of inflammation-induced E-EVs in the cell-to-cell communication between vascular endothelial cells and pericytes/vSMCs. Stimulation with inflammatory cytokines and endotoxin immediately induced release of shedding type E-EVs from the vascular endothelial cells, and flow cytometry showed that the induction was dose dependent. MiRNA array analyses revealed that group of miRNAs were specifically increased in the inflammation-induced E-EVs. E-EVs added to the culture media of cerebrovascular pericytes were incorporated into the cells. The E-EV-supplemented cells showed highly induced mRNA and protein expression of VEGF-B, which was assumed to be a downstream target of the miRNA that was increased within the E-EVs after inflammatory stimulation. The results suggest that E-EVs mediate inflammation-induced endothelial cell-pericyte/vSMC communication, and the miRNAs encapsulated within the E-EVs may play a role in regulating target cell function. E-EVs may be new therapeutic targets for the treatment of inflammatory diseases.

Cell-to-cell communication is mediated by secreted bioactive molecules, such as short form peptides, proteins, lipids, and nucleic acids. These small molecules are commonly released by cells and bind to specific receptors on target cells, which induces intracellular signaling and changes the target cell's pathophysiological state. Extracellular vesicles (EVs), which include microparticles, microvesicles, and exosomes[1–4], are released from different cell types, and emerging evidence suggests that EVs function as carriers of these bioactive molecules[5–8].

Clinically, EVs are found in circulating blood, and the number of EVs is elevated in acute and chronic inflammatory diseases, such as sepsis, stroke, preeclampsia, atherosclerosis, diabetes mellitus, and metabolic syndrome[9–14]. Vascular endothelial cells are thought to be one of the major cell types that release EVs into the blood stream[15]. The number of endothelial-derived EVs (E-EVs) circulating in the blood stream correlates with the severity of disease; however, the pathophysiological significance of E-EVs is largely unknown[12].

MicroRNAs (miRNAs) are small, single-stranded, non-coding RNAs that are transcribed in the nucleus. They are processed by the enzymes Drosha and Dicer, incorporated into RNA-induced silencing complexes, and mediate the translational inhibition or degradation of target mRNAs[16,17]. Many miRNAs have been shown to play key roles in pathophysiological processes[18,19]. In particular, the inflammation-related miRNAs, miR-101, miR-144, and miR-155, were reported to modulate protein biogenesis in lung epithelial and endothelial cells[20,21].

These miRNAs can be carried by E-EVs; however, their roles in E-EV-mediated cell-to-cell communication are not yet known.

Vascular endothelial cells and pericytes/vascular smooth muscle cells (vSMCs) are juxtapositioned to each other in blood vessels[22]. The interactions between these two cell types are important for the regulation of vascular integrity, and perturbation of their interaction has been observed in many diseases, including inflammatory diseases that cause vascular dysfunction, such as disturbance of the blood brain barrier (BBB) in cerebral blood vessels[23–26]. Here, we aimed to determine the involvement of EVs in cerebrovascular endothelial cell-pericyte communication in inflammatory disease. We found that the E-EVs induced by inflammatory stimuli carry numerous specific miRNAs and can induce pericyte responses to endothelial cells. These results suggest that E-EVs are an important mediator of vascular cell communication in inflammatory conditions.

Results

Induction of inflammatory responses in cerebrovascular endothelial cells. To analyze the pathobiology of E-EVs released in inflammatory conditions, we developed a reproducible *in vitro* system to induce the production of E-EVs from b.End5 cells, a cerebrovascular endothelial cell line. First, we confirmed that b.End5 cells expressed the LPS receptor TLR4/MD-2 complex under unstimulated conditions by immunocytofluorescence (Fig. 1a). The mRNAs of the inflammatory cytokine receptors *Tnfr1* (for TNF-α), *Il1r* (for IL-1β), and *Ifngr1* (for IFN-γ) were detected in unstimulated b.End5 cells by conventional RT-PCR (Fig. 1b). The gene expression levels were consistent up to 24 hours after stimulation with a high dose of CytoCombo + LPS (a mixture of TNF-α, IL-1β, IFN-γ, and LPS; Supplementary Table 1).

As inflammatory stimuli have been reported to upregulate IL-6 and ICAM-1 expression levels[27,28], we determined the inflammatory responses in b.End5 cells to inflammatory cytokine and endotoxin exposure by measuring *Il6* and *Icam1* gene expression. In real-time PCR analyses, a high dose of CytoCombo + LPS (Supplementary Table 1) induced *Il6* and *Icam1* mRNA expression, which peaked after 3 hours of stimulation (Fig. 1c and d). LPS alone also induced *Il6* and *Icam1* mRNA expression, but at lower levels than CytoCombo + LPS (Fig. 1c and d). In accordance with the *Icam1* mRNA expression (Fig. 1d), the immunoreactivity of ICAM-1 in b.End5 cells was detectable at 3 hours and peaked at 6 to 12 hours after CytoCombo + LPS stimulation (Fig. 1e).

To determine the optimal stimulatory conditions for inducing inflammatory responses in b.End5 cells, the dose effects of the inflammatory stimuli were determined by real-time PCR analyses of *Il6* and *Icam1* mRNA at 3 hours after stimulation. The expression of *Il6* and *Icam1* mRNA was significantly induced by CytoCombo + LPS, CytoCombo (a mixture of TNF-α, IL-1β, and IFN-γ), and LPS (Fig. 1f and g). However, the mRNA levels induced by CytoCombo + LPS were significantly higher than those induced by the other stimuli at all doses examined. The mRNA levels induced by the low and middle doses of LPS were significantly higher than those induced by the low and middle doses of CytoCombo, whereas the high doses of both stimuli induced equivalent mRNA expression levels (Fig. 1f and g). The induction of *Il6* and *Icam1* mRNA was not significant when b.End5 cells were stimulated with either cytokine alone. As an apoptotic cell death triggered by the inflammatory cytokines and LPS[29,30], has been reported to induce the release of apoptotic bodies[4], we examined apoptosis in b.End5 cells that were exposed to inflammatory stimuli. As compared with non-stimulated control, 3-hour exposure to any kinds of stimulants did not significantly increase the cleaved caspase 3-positive apoptotic cell. Twenty four-hour exposure to the stimulants except for that of low and middle dose of CytoCombo significantly increased cleaved caspase 3-positive apoptotic cell (Supplementary Figure 1a and b). Based on these data, we exposed b.End5 cells to CytoCombo + LPS, LPS, and CytoCombo for 3 hours when induction of apoptosis is still not evident, and then examined the inflammatory simulation-induced E-EV release from these cells.

Inflammation induced E-EV release from cerebrovascular endothelial cells. We next examined E-EV release from b.End5 cells that were stimulated by CytoCombo + LPS. To identify the E-EVs released from b.End5 cells, the plasma membranes of these cells were pre-labeled with PKH26 and these cells were then exposed to the inflammatory stimuli. Three hours after exposure to a high dose of CytoCombo + LPS, PKH26 fluorescence was detected on the plasma membrane of b.End5 cells (Fig. 2a, upper row). Then, we identified PKH26-positive objects of submicron to micron size within the E-EVs fractionated from the culture medium of PKH26-positive b.End5 cells after a 3-hour stimulation with the high dose of CytoCombo + LPS, and confirmed that these fractionated materials were b.End5-derived globules. We further characterized them using the extracellular vesicle markers, such as vascular endothelial growth factor receptor 2 (VEGFR-2) and CD62E (E-selectin)[31]. These globular objects in E-EV fraction were immunoreactive for VEGFR-2 and CD62E under confocal microscopy (Supplementary Figure 2). In addition, immunoreactive bands of VEGFR-2 and CD62E were enriched in the E-EV fraction than in b.End5 cell lysates by western blot analyses (Supplementary Figure 3).

The surface of the plasma membrane of the inflamed endothelial cells was examined by scanning electron microscopy (SEM). In most of unstimulated b.End5 cells (Initial), we observed few cellular processes like microvilli and limited number of sheddings on the surface of the plasma membrane (Fig. 2b, upper), whereas small fraction of unstimulated cells (2.38 ± 5.83%) showed similar changes as seen in those with stimulation. At 10 seconds after the addition of high dose CytoCombo + LPS to the culture medium, many sheddings were emerged on the surface of plasma membrane, and the microvilli turned to be obscure in all stimulated cells (100%; Fig. 2b, upper row). Higher magnification images further revealed the tiny and dome-shaped swellings (less than 0.1 μm in diameter) on the surface of plasma membrane, which structure may correspond to the early phase of sheddings (Supplementary Figure 4a). The sheddings were further increased at 10 minutes, and most of them ranged between 0.1 μm and 0.4 μm in diameter (Fig. 2b, upper row). At higher magnification, sheddings of larger-size (≥0.3 μm) and those of aggregated form (up to 3 μm) were increased as compared with those at 10-second of stimulation (Supplementary Figure 4b). In addition, similar shedding-like structures were observed on the bottom surface of the cells that were exposed to high-dose CytoCombo + LPS by using the interference contrast microscopy (DIC) mode of a confocal microscope (Fig. 2b, bottom row). These data strongly suggest that E-EV production is mainly membrane-shedding type[15,32] and may be partly from multivesicular bodies (MVBs)[33], and the plasma membrane shedding of E-EVs induced by inflammatory stimulants is very acute. In addition, our findings may support the possibility that E-EVs could be produced bilaterally, on both the luminal and abluminal surfaces, from inflammation-stimulated endothelial cells in cerebral blood vessels *in vivo*.

Next, E-EV release from b.End5 cells prelabeled with PKH26 was quantitatively analyzed by flow cytometry. Based on the above mentioned SEM study, we focused on particles between 0.3 μm and 3.0 μm in diameter, which corresponds to the diameter of the E-EVs released in membrane-shedding mode[32,34,35]. The preculture medium containing CytoCombo + LPS included many particles between 0.3 μm and 3.0 μm in diameter that were negative for PKH26, such as FBS-derived EVs, and EVs from MVBs (Fig. 3a, upper graphs). In contrast, after 3 hours of culture with high dose CytoCombo + LPS, the culture medium contained a significant number of PKH26-positive particles between 0.3 μm and 3.0 μm in diameter (Fig. 3a, bottom graphs). These findings indicated that the plasma membrane-intercalating nature of PKH26, with which

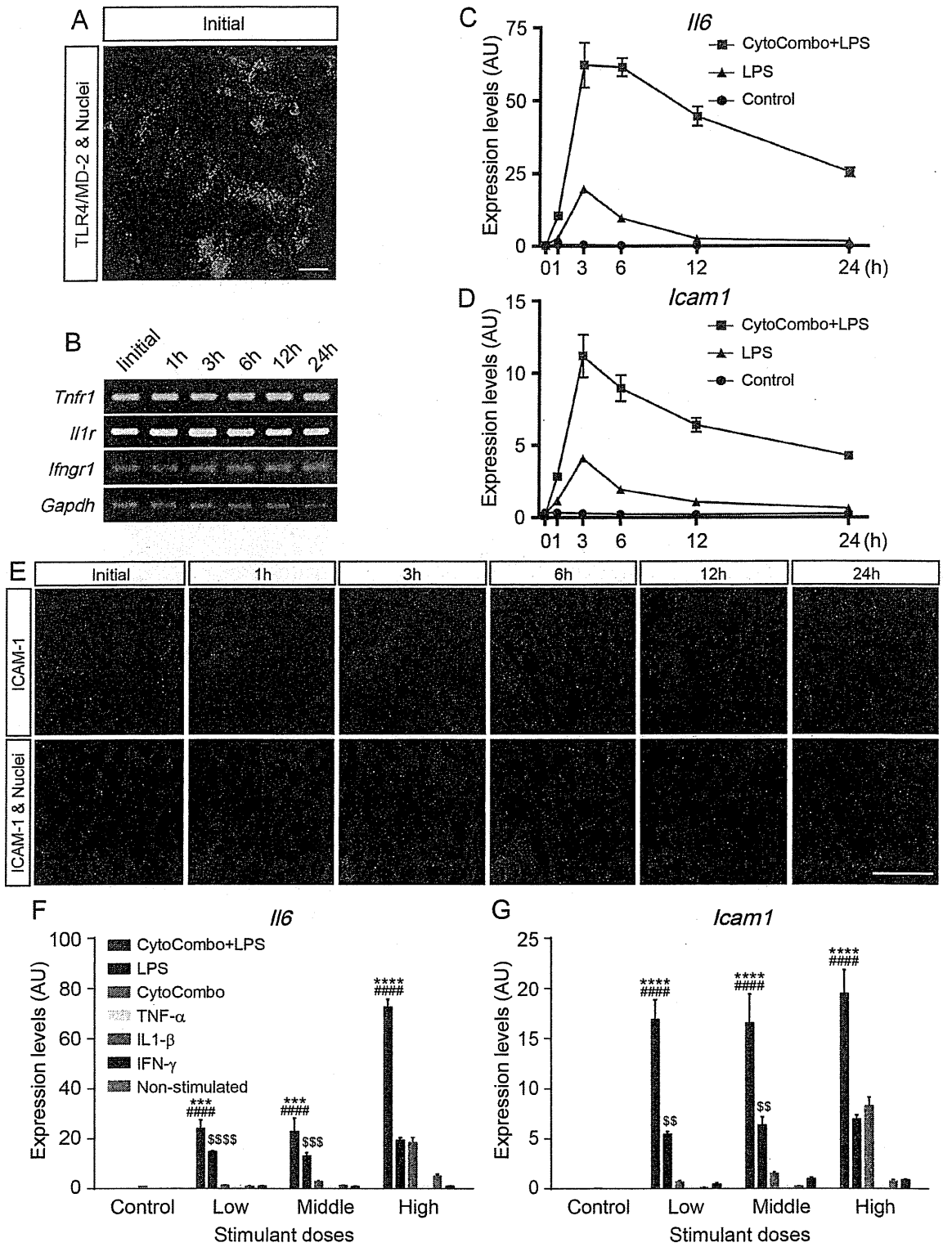

Figure 1 | Inflammation-related receptor gene and protein expression levels in cerebrovascular endothelial cells. (a) Expression of the TLR4/MD-2 protein complex was confirmed by immunocytofluorescence (Green). Unstimulated b.End5 cells constitutively express the TLR4/MD-2 protein complex. Nuclei are stained with Hoechst (Blue). Scale bar, 10 μm. (b) Analysis of *Tnfr1*, *Il1r*, and *Ifngr1* expression by conventional RT-PCR. Unstimulated b.End5 cells constitutively express *Tnfr1*, *Il1r*, and *Ifngr1*, and these genes are continuously expressed after 24 hours of stimulation with CytoCombo + LPS. (c and d) Inflammatory gene expression levels in b.End5 cells. *Il6* (c) and *Icam1* (d) are markers of inflammatory responsive genes (n = 4 for each time point). Both genes peaked at 3 hours after stimulation. (e) ICAM-1 protein expression levels were confirmed by immunocytofluorescence. ICAM-1 protein expression levels were well correlated with the *Icam1* mRNA expression pattern. Scale bars, 50 μm. (f and g) Inflammatory gene expression levels in b.End5 cells incubated with various stimulants. The inflammatory responsive genes *Il6* (f) and *Icam1* (g) were measured at 3 hours after stimulation (n = 4 for each time point). Cells stimulated with CytoCombo + LPS showed the most intensive inflammation. Non-stimulated control indicates basal expression level of marker genes. **** $P < 0.0001$, and *** $P < 0.001$, CytoCombo + LPS *vs.* LPS; $^{\#\#\#\#}P < 0.0001$, CytoCombo + LPS *vs.* CytoCombo; $^{\$\$\$\$}P < 0.0001$, $^{\$\$\$}P < 0.001$, and $^{\$\$}P < 0.01$, LPS *vs.* CytoCombo.

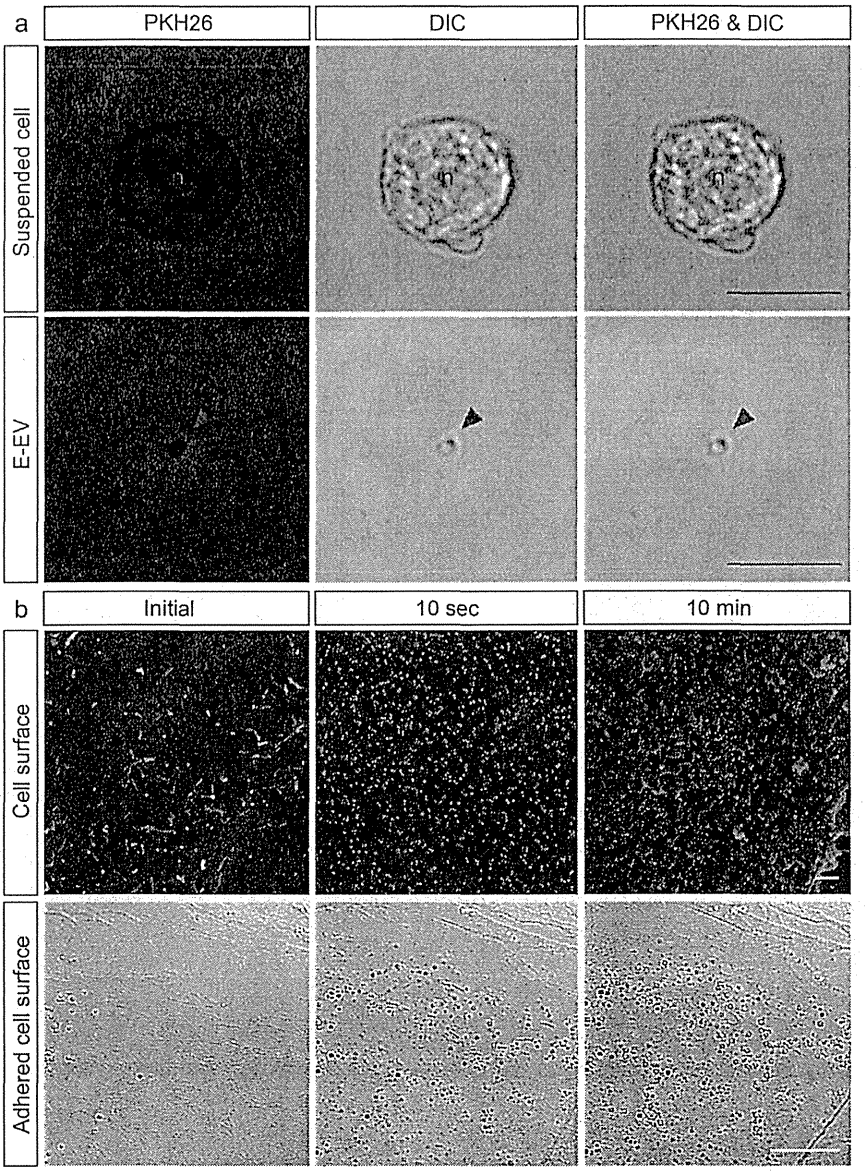

Figure 2 | Inflamed cerebrovascular endothelial cells produce shedding-type E-EVs. (a) Treatment of inflamed cells with PKH26, a plasma membrane-intercalating fluorescent reagent, clearly demonstrates that E-EVs are released from the inflamed endothelial cell membranes. Suspended b.End5 cells stained with PKH26 emit red fluorescence (Upper row). Azure-blue n indicates nucleus. PKH26-positive E-EVs are present in the culture medium (Bottom row). Red fluorescence is colocalized to the micron-sized vesicles as observed by differential interference contrast microscopy (DIC). The azure-blue arrowhead shows an E-EV. Scale bar, 10 μm. (b) Scanning electron microscopy (SEM) images showing that E-EVs are shed from the cell surface immediately after stimulation by CytoCombo + LPS (Upper row). The acute response implies that E-EV production is a non-genomic reaction. DIC image showing E-EVs present on the adhered cell surface (Bottom row), suggesting that E-EVs are bilaterally produced on both the luminal and abluminal surfaces of endothelial cells in the tube formed by the blood vessels in inflammatory conditions *in vivo*. Scale bar, 10 μm (a and b lower), and 1 μm (b upper).

the b.End5 cells were prelabeled, allowed us to discriminate foreign substances in the medium from E-EVs and to precisely measure the release of E-EVs. In a comparative assay, the three types of stimulants significantly induced the release of PKH26-positive E-EVs compared to that released from the non-stimulated control (stimulant, P-value *vs.* the control; CytoCombo + LPS, $P < 0.0001$; CytoCombo, $P < 0.01$; LPS, $P < 0.05$; Fig. 3b). CytoCombo + LPS induced the release of E-EVs in a dose-dependent manner up to the high dose, and the release induced by CytoCombo + LPS was significantly higher than that induced by the other stimuli at the high dose (Fig. 3b). At the high doses, CytoCombo and LPS individually induced the release of E-EVs to similar extents. These changes of E-EV production were well correlated with those of *Il6* and *Icam1* mRNA induction, both of which were induced by different inflammatory stimuli. Accordingly, these data suggested that E-EV production was correlated with the level of cellular inflammation. At the low and middle doses, CytoCombo induced E-EV release ($P < 0.01$ and $P < 0.001$, respectively, *vs.* the control) but not *Il6* and *Icam1* mRNA (both n.s. *vs.* the control; Fig. 1f and g). Thus, E-EV production in cerebrovascular endothelial cells appears to be a more sensitive cellular response than cytokine production based on relative induction by inflammatory stimulants.

Inflammation-induced E-EVs may target cerebrovascular pericytes. Endothelial cells and pericytes are juxtapositioned and functionally correlated in the vasculature[22,36]. Next, we determined if the miRNAs in E-EVs could mediate the inflammatory signaling between cere-

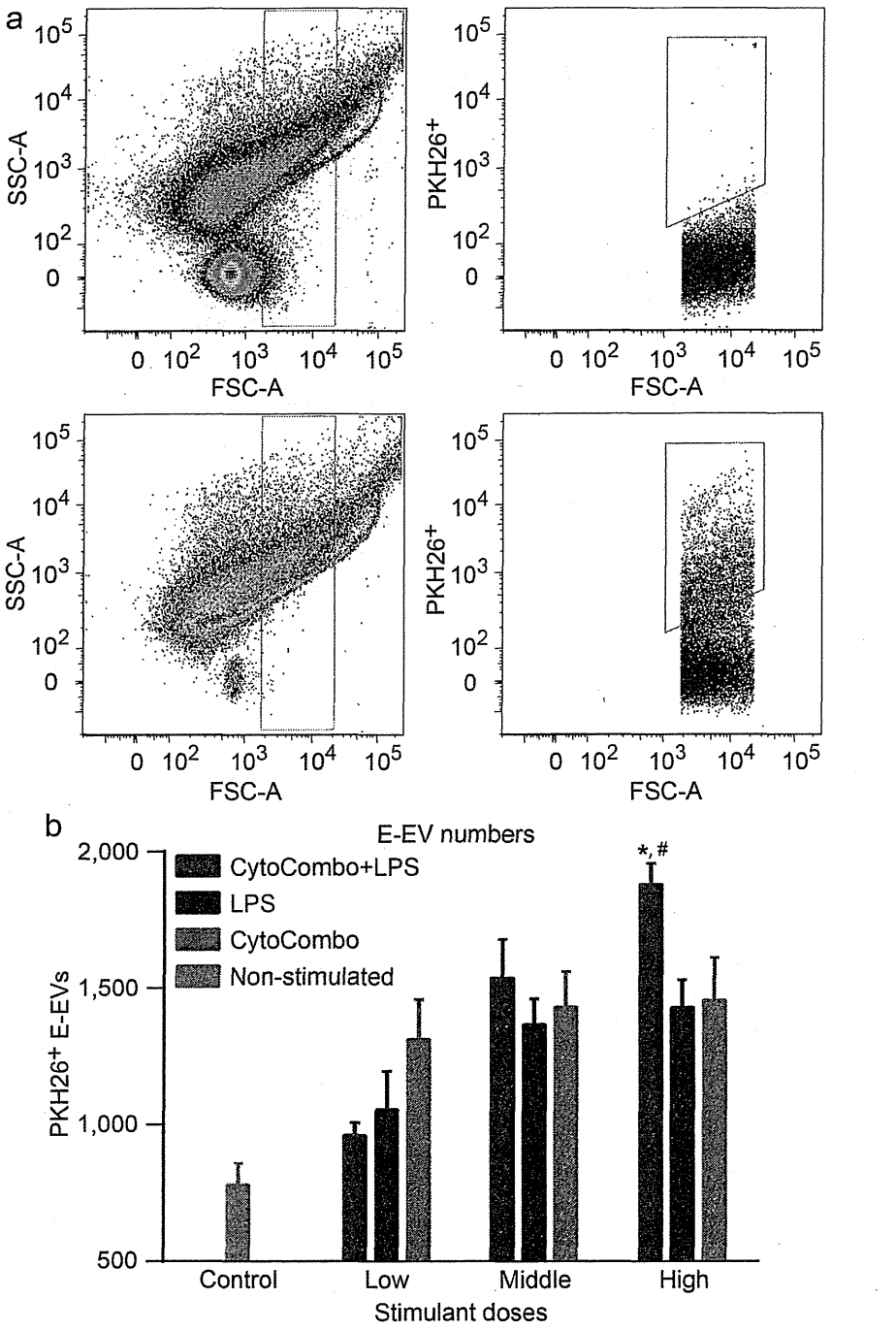

Figure 3 | Quantitative analysis of E-EVs by flow cytometry. (a) PKH26-positive E-EVs were detected and measured quantitatively by flow cytometry. The upper graphs show the pre-culture medium with CytoCombo + LPS. The lower graphs show the culture medium from b.End5 cells stained with PKH26 stimulated by CytoCombo + LPS for 3 hours. Vesicles gated from submicron to micron size (0.3 μm to 3.0 μm in diameter, magenta) are shown in the graph on the left. In the graphs on the right, PKH26-positive E-EVs are gated (red). The pre-culture medium contains many FBS-derived vesicles that are negative for PKH26. E-EVs can be observed in the 3-hour culture medium as the PKH26-positive fraction. (b) E-EV production is significantly upregulated after 3 hours of exposure to the high dose of CytoCombo + LPS. In contrast, a lower number of E-EVs are observed in the LPS and CytoCombo groups (reported as the number of PKH26-positive E-EVs in 100 μL of medium, n = 4 for each). Non-stimulated control indicates basal production level of E-EVs. * $P < 0.05$, CytoCombo + LPS *vs.* LPS; #$P < 0.05$, CytoCombo + LPS *vs.* CytoCombo.

brovascular endothelial cells and pericytes. To this end, we first assessed whether E-EVs could be incorporated into pericytes. To rule out the effect of modification to the E-EV surface by the plasma membrane-intercalating dye PKH26, we constructed a membrane-localized EGFP (M-EGFP)-coding vector. M-EGFP-positive E-EVs were fractionated from the culture medium of M-EGFP expressing b.End5 cells after a 3-hour stimulation with the high dose of CytoCombo + LPS. The E-EV fractions obtained were washed 3 times with PBS, and then added to the culture medium of human brain pericytes (HBPCs). After a 24-hour incubation, immunocytofluorescence showed that many M-EGFP-positive E-EVs were incorporated into the cytoplasmic region of HBPCs (Fig. 4). Some of the M-EGFP-positive E-EVs were localized near the nucleus, as confirmed by the Y-Z cross-sectional image and single-plane

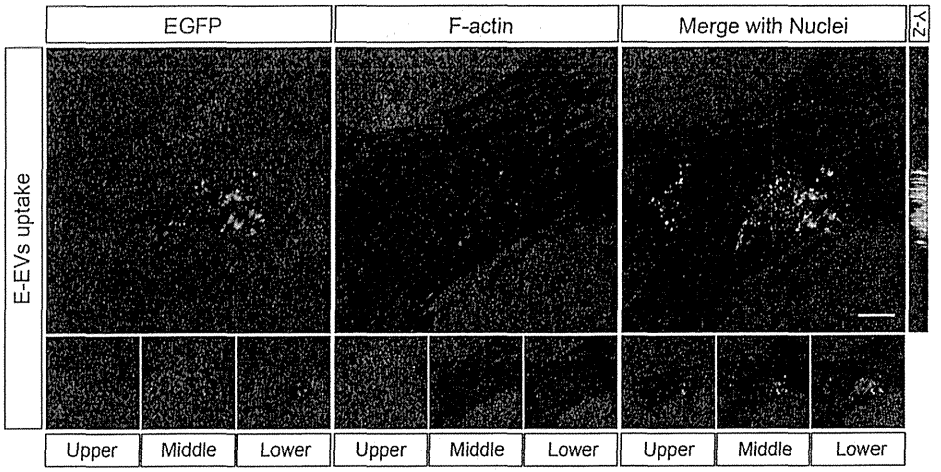

Figure 4 | E-EVs are incorporated into cerebrovascular pericytes. Plasma membrane-localized EGFP (M-EGFP)-positive E-EVs were fractionated from M-EGFP-expressing b.End5 cells. When the M-EGFP-positive E-EVs were incubated with cerebrovascular pericytes, the E-EVs were taken up by the cells as confirmed by immunocytofluorescence of EGFP. Incorporation of the E-EVs by the cells was precisely confirmed by a Y-Z cross-sectional image (adjacent to the 3D projection merged image) and by 1-μm, sequential, single Z-plane images (bottom row). Scale bar, 10 μm.

sequential Z images (Fig. 4, upper right and bottom row). These findings suggest that the bioactive molecules encapsulated in the E-EVs were transferred into HBPCs.

To examine the bioactive molecules encapsulated in the E-EVs, we examined the molecules in the E-EV fractions from b.End5 cells with an miRNA array. Many miRNAs were upregulated in the E-EVs from cells stimulated by a high dose of CytoCombo + LPS compared to those in the E-EVs from non-stimulated control cells (Fig. 5a). Some of them were also upregulated in the E-EVs from cells stimulated with a high dose of CytoCombo, which induced an inflammatory response in b.End5 cells, although to a lesser extent than CytoCombo + LPS (Fig. 5a). These miRNAs sorted into the E-EVs were classified by Ingenuity Pathway Analysis (IPA). A significant proportion of the miRNAs were approved to be related to Inflammatory Disease and Inflammatory Response (bright red) in Disease and Disorders of the IPA (Supplementary Figure 5). Moreover, the miRNAs were abundant in those related to Organismal Injury and Abnormalities, which may associate with inflammation, over-represented (dark red). These data suggest that inflammatory stimuli are able to sort the inflammation-related miRNAs into E-EVs.

Among the various inflammation-related miRNAs detected (Fig. 5a), we focused on two, miR-328-3p and let-7d-3p, because these miRNAs were extensively induced after stimulation with CytoCombo + LPS, and were significantly induced, but to a lesser extent, after CytoCombo stimulation. Real-time PCR showed that the cultured HBPCs expressed *Yin and yang 1* (*YY1*), which is a target mRNA of let-7d-3p and is an orthologue of mouse *Yy1* that was identified through in silico analysis (Figure 5b), but not the target mRNAs of miR-328-3p including *Proviral integration site for Moloney murine leukemia virus 1* (*PIM1*), *Testis-specific kinase 2* (*TESK2*), and *Ataxin-2 binding protein 1* (*A2BP1*) (data not shown). The well-conserved, mature let-7d-3p sequences in mice and humans are identical (Fig. 5c) and were shown to target *YY1* mRNA through *in silico* analyses (Fig. 5d). VEGF family proteins are synthesized in pericytes/vSMCs[37,38] and are believed to be the downstream targets of *YY1*, since *YY1* knockdown upregulates their expression levels, in which the upregulation of VEGF-B was most striking among VEGF family proteins[39]. Therefore, we investigated whether inflammation-induced E-EVs modulated the expression of VEGF family mRNAs and proteins. We observed that VEGF-B mRNA and protein levels were low in the controls, but were extensively induced in the E-EV-supplemented group (Fig. 6b, e, f). In contrast, E-EV supplementation did not affect *VEGFA*, *VEGFC*, or *PLGF* mRNA levels (Fig. 6a, c, d). The miRNAs carried by E-EVs may mediate the inflammatory responses of endothelial cells by regulating gene expression profiles in pericytes/vSMCs, especially in cerebrovascular pericytes.

Discussion

Emerging evidence has suggested the importance of EVs in cell-to-cell communication as carriers of small molecules such as peptides, proteins, lipids, mRNAs, and miRNAs[40,41]. The bioactive molecules encapsulated in EVs can be transferred to and function in target recipient cells[6,42–44]. In addition, miRNAs act as regulatory molecules of diverse biological phenomena, such as immune responses, inflammation, and tumor growth[18,19]. However, our knowledge of EV- and encapsulated miRNA-mediated cell-to-cell communication is mainly limited to tumor cell biology. Although it is known that the proinflammatory agent TNF-α induces the release of E-EVs[45], the significance of these E-EVs remains to be elucidated. To the best of our knowledge, we demonstrated here, for the first time, that the inflammation-related miRNAs carried by the E-EVs from endothelial cells mediated inflammatory responses in pericytes. The induction of E-EV shedding was very acute and sensitive compared to previously established inflammation markers like IL-6 and ICAM-1[27,28], and it may be useful as a very sensitive marker for inflammatory diseases.

In recent years, a variety of pathogens and disease states have been shown to affect the composition and function of these EVs. *In vitro* studies demonstrated that environmental stresses such as heat, hypoxia, irradiation, and changing of conditioned medium, differentially modified the composition of EVs[46–49]. Specific coding and non-coding RNAs, retrotransposon RNAs, Alu transposable elements, and chromosomal and mitochondrial DNA have been reported to be enriched in tumor cell-derived EVs[50–54]. The results of our present study showed that when exposed to inflammatory stimuli, cerebrovascular endothelial cells could sort many inflammation-related miRNAs into E-EVs *ad initium*. Moreover, the type and amount of miRNAs that were sorted into the E-EVs was strongly correlated with the severity of endothelial inflammation.

EVs from tumor cells could educate the bone marrow progenitor cells to mobilize out from their niche[55]. Vascular endothelial cells in tumors could be "educated" by EVs derived from tumor cells to exhibit a highly proliferative phenotype and karyotype abnormalities[7,56]. Along these same lines, our results show that the molecules in the inflammation-induced E-EVs function in target pericytes to increase

a

Without stimulant (control)	
Systematic_name	Raw
mmu-miR-328-3p	0.100
mmu-miR-211-5p	0.100
mmu-let-7d-3p	0.100
mmu-miR-698-3p	0.100
mmu-miR-204-5p	0.100
mmu-miR-615-3p	0.100
mmu-miR-485-3p	0.100
mmu-miR-764-5p	0.100
mmu-miR-335-3p	0.100
mmu-miR-346-5p	0.100
mmu-miR-18a-3p	0.100
mghv-miR-M1-9	0.100
mmu-miR-329-3p	0.100
mmu-miR-540-5p	0.100
mmu-let-7c-1-3p	0.100
mmu-miR-130b-5p	0.100
mmu-miR-29c-5p	0.100
mmu-miR-1900	0.100
mcmv-miR-m59-2	0.100
mghv-miR-M1-7-3p	0.100
mmu-miR-34b-3p	0.100
mmu-miR-191-3p	0.100
mmu-miR-1193-3p	0.100
mmu-let-7a-1-3p	0.100
mmu-miR-511-5p	0.100
mmu-miR-351-5p	0.100
mmu-miR-434-3p	0.100
mmu-miR-92b-3p	0.100
mmu-miR-299a-5p	0.100
mmu-miR-154-5p	0.100
mmu-miR-1190	0.100
mmu-let-7g-3p	0.100
mmu-miR-340-3p	0.100
mmu-miR-26b-3p	0.100
mmu-miR-193b-3p	0.100
mmu-miR-199a-5p	0.100
mmu-miR-199b-5p	0.100
mmu-miR-744-3p	0.100
mmu-miR-880-3p	0.100
mmu-miR-683	0.100
mmu-miR-10b-5p	0.100
mmu-miR-343	0.100
mmu-miR-467a-3p	0.100
mmu-miR-324-3p	0.100
mmu-miR-326-3p	0.100
mmu-miR-342-3p	0.100
mmu-miR-291a-3p	0.100
mmu-miR-423-3p	0.100
mmu-miR-668-3p	0.100
mmu-miR-675-3p	0.100
mmu-let-7i-3p	0.100

CytoCombo		
Systematic_name	Raw	Fold change vs. control
mmu-miR-328-3p	10.657	106.566
mmu-miR-211-5p	0.100	1.000
mmu-let-7d-3p	6.358	63.576
mmu-miR-698-3p	0.100	1.000
mmu-miR-204-5p	0.100	1.000
mmu-miR-615-3p	0.100	1.000
mmu-miR-485-3p	0.100	1.000
mmu-miR-764-5p	0.100	1.000
mmu-miR-335-3p	0.100	1.000
mmu-miR-346-5p	0.100	1.000
mmu-miR-18a-3p	0.100	1.000
mghv-miR-M1-9	0.100	1.000
mmu-miR-329-3p	0.100	1.000
mmu-miR-540-5p	0.100	1.000
mmu-let-7c-1-3p	0.100	1.000
mmu-miR-130b-5p	0.100	1.000
mmu-miR-29c-5p	0.100	1.000
mmu-miR-1900	0.100	1.000
mcmv-miR-m59-2	31.634	316.337
mghv-miR-M1-7-3p	0.100	1.000
mmu-miR-34b-3p	0.100	1.000
mmu-miR-191-3p	5.504	55.040
mmu-miR-1193-3p	0.100	1.000
mmu-let-7a-1-3p	0.100	1.000
mmu-miR-511-5p	0.100	1.000
mmu-miR-351-5p	0.100	1.000
mmu-miR-434-3p	0.100	1.000
mmu-miR-92b-3p	0.100	1.000
mmu-miR-299a-5p	0.100	1.000
mmu-miR-154-5p	0.100	1.000
mmu-miR-1190	0.100	1.000
mmu-let-7g-3p	0.100	1.000
mmu-miR-340-3p	0.100	1.000
mmu-miR-26b-3p	0.100	1.000
mmu-miR-193b-3p	0.100	1.000
mmu-miR-199a-5p	0.100	1.000
mmu-miR-199b-5p	0.100	1.000
mmu-miR-744-3p	0.100	1.000
mmu-miR-880-3p	0.100	1.000
mmu-miR-683	0.100	1.000
mmu-miR-10b-5p	0.100	1.000
mmu-miR-343	0.100	1.000
mmu-miR-467a-3p	0.100	1.000
mmu-miR-324-3p	0.100	1.000
mmu-miR-326-3p	0.100	1.000
mmu-miR-342-3p	0.100	1.000
mmu-miR-291a-3p	0.100	1.000
mmu-miR-423-3p	5.225	52.253
mmu-miR-668-3p	0.100	1.000
mmu-miR-675-3p	0.100	1.000
mmu-let-7i-3p	0.100	1.000

CytoComb+LPS		
Systematic_name	Raw	Fold change vs. control
mmu-miR-328-3p	148.389	1483.887
mmu-miR-211-5p	108.716	1087.159
mmu-let-7d-3p	63.206	632.059
mmu-miR-698-3p	58.043	580.426
mmu-miR-204-5p	56.464	564.642
mmu-miR-615-3p	53.197	531.974
mmu-miR-485-3p	53.159	531.587
mmu-miR-764-5p	41.045	410.451
mmu-miR-335-3p	41.014	410.144
mmu-miR-346-5p	38.699	386.992
mmu-miR-18a-3p	37.589	375.892
mghv-miR-M1-9	36.071	360.707
mmu-miR-329-3p	32.767	327.668
mmu-miR-540-5p	32.184	321.840
mmu-let-7c-1-3p	30.890	308.901
mmu-miR-130b-5p	28.741	287.413
mmu-miR-29c-5p	28.676	286.764
mmu-miR-1900	28.277	282.772
mcmv-miR-m59-2	27.802	278.016
mghv-miR-M1-7-3p	26.648	266.483
mmu-miR-34b-3p	26.576	265.758
mmu-miR-191-3p	26.573	265.730
mmu-miR-1193-3p	26.315	263.146
mmu-let-7a-1-3p	25.464	254.640
mmu-miR-511-5p	23.639	236.394
mmu-miR-351-5p	22.977	229.771
mmu-miR-434-3p	22.793	227.931
mmu-miR-92b-3p	22.285	222.850
mmu-miR-299a-5p	22.142	221.417
mmu-miR-154-5p	22.076	220.762
mmu-miR-1190	21.848	218.485
mmu-let-7g-3p	13.368	133.682
mmu-miR-340-3p	13.246	132.461
mmu-miR-26b-3p	12.872	128.721
mmu-miR-193b-3p	11.567	115.668
mmu-miR-199a-5p	11.354	113.544
mmu-miR-199b-5p	11.262	112.616
mmu-miR-744-3p	10.709	107.090
mmu-miR-880-3p	9.940	99.397
mmu-miR-683	9.874	98.744
mmu-miR-10b-5p	9.846	98.459
mmu-miR-343	9.684	96.840
mmu-miR-467a-3p	9.128	91.282
mmu-miR-324-3p	8.924	89.238
mmu-miR-326-3p	8.835	88.351
mmu-miR-342-3p	8.692	86.922
mmu-miR-291a-3p	7.466	74.665
mmu-miR-423-3p	5.231	52.310
mmu-miR-668-3p	5.132	51.318
mmu-miR-675-3p	5.019	50.188
mmu-let-7i-3p	4.675	46.746

b

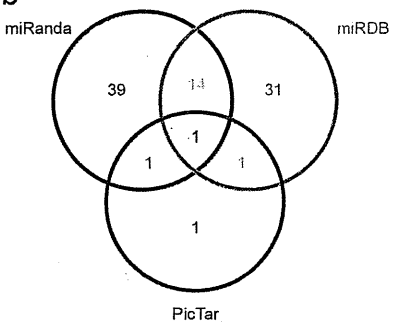

Gene symbol	Function
Yy1	Repressing and activating a diverse number of promoters

c

Human	CUAUACGACCUGCUGCCUUUCU
Pig	CUAUACGACCUGCUGCCUUUCU
Mouse	CUAUACGACCUGCUGCCUUUCU
Rat	CUAUACGACCUGCUGCCUUUCU
Chinese hamster	CUAUACGACCUGCUGCCUUUCU
	**********

d

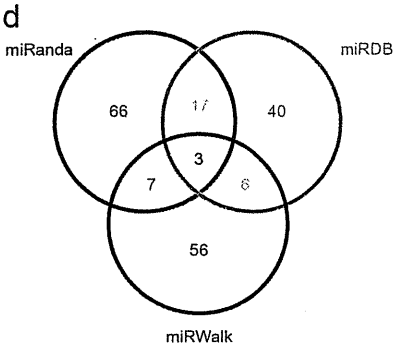

Gene symbol	Function
YY1	Repressing and activating a diverse number of promoters
ABCA8	Mitochondrial membrane ABC transporter
RLN2	Remodeling of connective tissues during pregnancy

Figure 5 | MiRNA array data from inflammation-stimulated E-EVs. (a) MiRNAs extracted from E-EVs undergo a drastic change following treatment with inflammatory stimulants. Some of the miRNAs are upregulated more than 500 fold by CytoCombo + LPS treatment when compared to the non-stimulated control. (b) The multifunctional transcription factor *Yy1* is determined as a target of let-7d-3p in mice that are commonly identified in 3 different public accessible databases. (c) Homology analysis of let-7d-3p. The alignment of let-7d-3p sequences indicates that the mature sequences of five mammalian species are identical. (d) *YY1, ABCA8,* and *RLN2* are determined as a target of let-7d-3p in human that are commonly identified in 3 different public accessible databases.

VEGF-B mRNA and protein expression. Furthermore, this "education" was suggested to be mediated by the miRNA encapsulated in the E-EVs since *VEGFB* is thought to be a downstream target of the highly-accumulated miRNA in the inflammation-induced E-EVs. Similarly, various organ-derived EVs have been shown to be incorporated into bone marrow cells *in vitro*[57]. As a result, the mRNAs were delivered and the expression of organ-specific mRNAs was induced in the bone marrow cells. E-EVs and encapsulated miRNA were shown to be involved in the cascade of cellular events in the inflammatory vascular response.

VEGF-B is a specific ligand of VEGFR-1 that is expressed in endothelial cells and pericytes/vSMCs[58,59]. VEGFR-1 mediates pathological angiogenesis by targeting both endothelial cells and pericytes in the pathological neovascularization of choroidal and retinal tissues[60]. Similarly, VEGFR-1 stimulates the endothelial differentiation and the formation of blood vessels in infantile hemangioma[61] and vascular formation in implanted tumors[62]. Furthermore, VEGFR-1 ablated vascular pericytes and aggravated vascular leakage to induce cancer-associated retinopathy[63]. Accordingly, inflammation-induced E-EVs enhanced VEGF-B expression in pericytes, which may mediate pathological neovascularization and/or vascular leakage in response to inflammation of endothelial cells. Furthermore, since E-EVs are carried in the blood stream in many pathological conditions, E-EVs may spread the local inflammatory responses of endothelial cells to the systemic vasculature. Inhibition of E-EVs may limit the extent of inflammation-induced cellular responses from endothelial cells to the surrounding cells, and E-EVs may be a new therapeutic target for inflammatory diseases.

In conclusion, we developed a reproducible *in vitro* E-EV production system and a quantitative E-EV measurement method. Using these tools, we demonstrated that inflammation-induced E-EVs could "educate" target cells to modulate growth factor production. We also showed evidence to suggest that part of this cell education signal might be an miRNA encapsulated in the E-EVs. Our findings offer a new clinical approach, targeting E-EVs, for the prevention and treatment of acute and chronic inflammatory diseases. Further experiments are needed to elucidate the molecular mechanisms by which E-EVs transfer their "educating" messages.

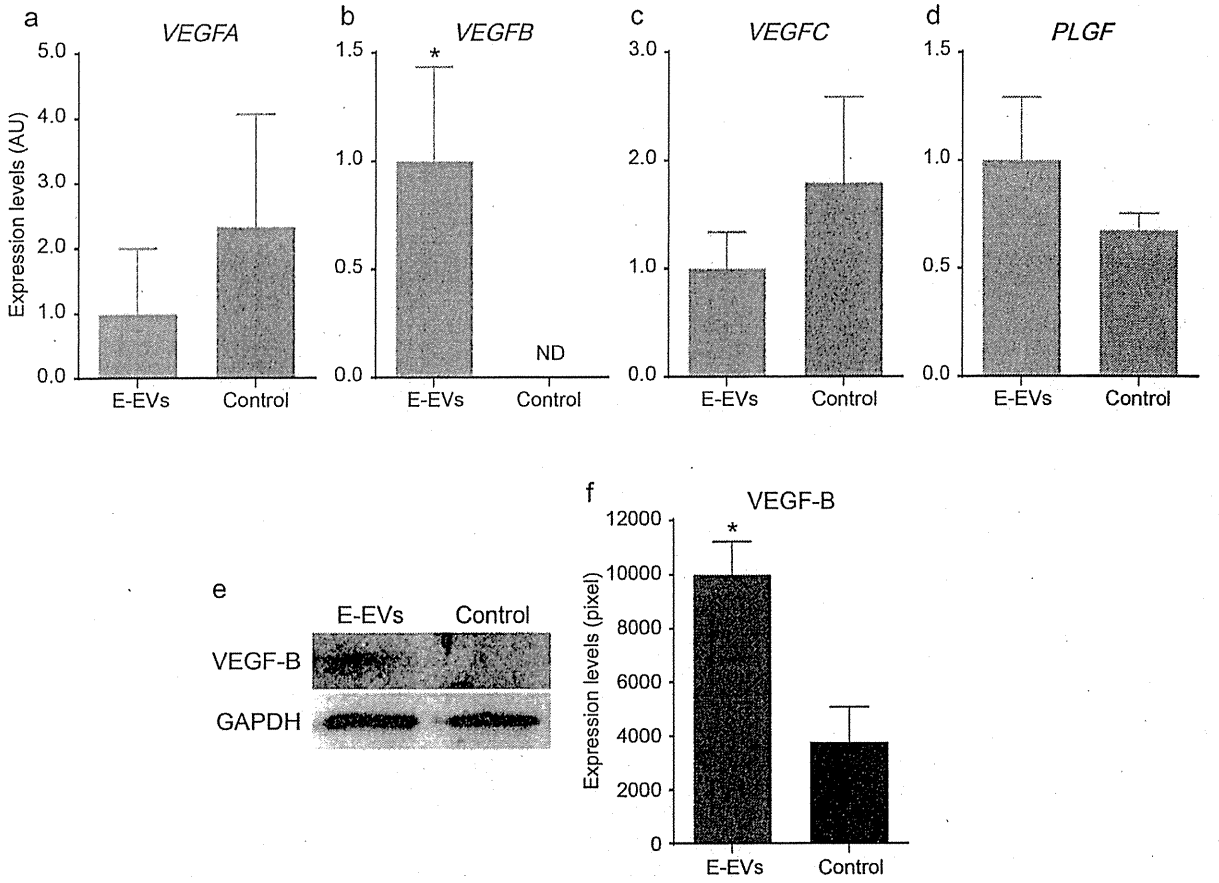

Figure 6 | Effects of E-EVs in cerebrovascular pericytes. (a–d) The mRNA levels of the VEGF family members, *VEGFA*, *VEGFC*, and *PLGF* in the E-EV-supplemented and non-stimulated control groups did not differ significantly (a, c, and d). In contrast, *VEGFB* was significantly upregulated in the E-EV-supplemented group compared to the non-stimulated control group (b) ($n = 3$, $P < 0.05$). (e and f) VEGF-B protein levels were measured by western blotting (e), using GAPDH as an internal control. VEGF-B protein was significantly upregulated in the E-EV-supplemented group compared to the non-stimulated control group (f) ($n = 3$, $P < 0.05$).

Methods

Cell lines and culture conditions. The mouse brain endothelial cell line, b.End5, and human brain pericytes (HBPCs) were purchased from DS Pharma Biomedical (Osaka, Japan), and from Applied Cell Biology Research Institute (Kirkland, WA), respectively. The cells were cultured using the EBM-2 bullet kit (Takara, Kyoto, Japan) at 37°C in a humidified atmosphere containing 5% CO_2. Membrane-localized EGFP (M-EGFP)-expressing b.End5 cells were generated by transfection of the *GAP43 membrane targeting sequence-Egfp* fusion gene, which was constructed as follows. Briefly, the human *GAP43 membrane targeting sequence* was cloned from the plasmid (Clone ID No. IRAL020F10, RIKEN BRC, Tsukuba, Japan) and inserted into the multi-cloning site of the pEGFP-N1 vector (Takara). The vector containing the resultant fusion gene, consisting of the *GAP43 membrane targeting sequence* and *Egfp*, was transfected into b.End5 cells using X-tremeGENE transfection reagent (Roche, Basel, Switzerland) according to the manufacturer's protocol.

Reagents. The inflammatory cytokines TNF-α, IL-1β, and IFN-γ were purchased from PeproTech (Rocky Hill, NJ). Lipopolysaccharide (LPS) was obtained from List Biological Laboratories (Campbell, CA). TNF-α, IL-1β, and IFN-γ were used separately, as a mixture (referred to as CytoCombo), or as a mixture of CytoCombo and LPS (CytoCombo + LPS) (Supplementary Table 1). The plasma membrane intercalating fluorescent dye PKH26 was purchased from Sigma-Aldrich (St. Louis, MO) and was used according to the manufacturer's protocol. The cell tracer fluorescence dye 5-(and 6)-carboxyfluorescein diacetate succinimidyl ester (CSFE) was purchased from eBioscience (San Diego, CA) and was used according to the manufacturer's protocol.

Fractionation of endothelial cell-derived extracellular vesicles (E-EVs). Ten-centimeter dishes coated with type I collagen (BD Biosciences, San Jose, CA) of confluent b.End5 cells were rinsed with PBS, and stimulated with medium containing CytoCombo + LPS, CytoCombo, or LPS alone to induce inflammation. Culture medium without any stimulant was used as a control. After a 3-hour incubation, the conditioned culture medium was centrifuged at 1,000 rpm for 10 minutes at 4°C to eliminate the cellular debris. The supernatant was then ultracentrifuged at 100,000 × *g* for 90 minutes at 4°C, and the pellets were used as the E-EV fraction in the following analyses.

Immunocytofluorescence. For immunocytofluorescence, cells were seeded into 8-well culture slides (BD Biosciences). After treatment with various stimuli, the slides were fixed in 4% paraformaldehyde for 15 minutes on ice, and then rinsed with PBS. All specimens were permeabilized in a 0.3% Triton X-100/PBS solution. Permeabilized specimens were incubated at 4°C overnight with primary antibodies diluted in 0.03% Triton X-100/PBS with 10% normal goat serum (VECTOR LABORATORIES, Burlingame, CA), which was used for blocking. The following primary antibodies were used: rat anti-TLR4/MD-2 complex (1 : 200; eBioscience), mouse anti-ICAM-1 (1 : 200; Abcam, Cambridge, UK), rabbit anti-cleaved caspase 3 (1 : 200; Cell Signaling Technology, Danvers, MA), rabbit anti-GFP (1 : 100; Frontier Institute, Hokkaido, Japan). The Alexa-Fluor488, Alexa-Fluor568, or Alexa-Fluor633-conjugated secondary antibodies (Life Technologies Corporation, Carlsbad, CA) were used at 1 : 500 dilutions. For F-actin staining, Falloidin-Alexa-Fluor647 (1 : 500; Cytoskeleton, Denver, CO) was used. Nuclei were stained with Hoechst 33258 (Nacalai Tesque, Koto, Japan). For immunofluorescence of E-EVs, fractionated E-EVs from culture media of b.End5 cells pre-stained by PKH26 or CSFE were incubated with 3% normal mouse serum (VECTOR LABORATORIES) at 4°C for blocking. The following primary antibodies were used: rat anti-Flk-1-FITC (1 : 20; BD Biosciences, San Jose, CA), rat anti-CD62E-PE (1 : 20; BD Biosciences). The imaging system was a Leica TCS SP5 confocal system (Leica Microsystems, Wetzlar, Germany).

FACS analysis. E-EVs released into culture media were analyzed by flow cytometry. E-EVs in the media were gated as events of 0.3 to 3.0 μm in diameter, corresponding to the size of the membrane shed EVs[32–34]. E-EVs were further gated as PKH26-positive events, by using b.End5 cells pre-labeled with PKH26, a membrane intercalating dye. This gating allowed us to discriminate E-EVs from the other microparticles of similar diameters in the medium. We used 3.0- to 3.4-μm rainbow calibration particles (BD Biosciences) as benchmarks. Flow cytometry was performed with a FACSCanto II (BD Biosciences) and FlowJo software (Tree Star, Ashland, OR) was used for data analysis.

Scanning electron microscopy. Endothelial b.End5 cells were seeded on cover slips and cultured until confluent. Confluent cells were then exposed to inflammatory stimuli (CytoCombo + LPS) for 10 seconds or 10 minutes. After stimulation, the cells were fixed with 2% formaldehyde (Wako Pure Chemical Industries, Osaka, Japan) and 2.5% glutaraldehyde (Wako Pure Chemical Industries) prepared in 0.1 M sodium phosphate buffer (pH 7.4) for 2 hours at room temperature, and then postfixed in 1% osmium tetroxide in the same buffer for 2 hours on ice. Cells were then dehydrated in a graded series of ethanol, substituted with t-butyl alcohol and freeze-dried. Cells were sputter-coated with osmium and then observed in a S4200 scanning electron microscope (Hitachi).

RNA extraction, cDNA synthesis, conventional PCR, and real-time PCR. Total RNA was isolated from b.End5 cells or HBPCs using the RNeasy Mini Kit (Qiagen, Hilden, Germany) according to the manufacturer's instructions. Total RNA (100 ng) was reverse-transcribed as described in the PrimeScript RT reagent Kit protocol (Takara). Conventional PCR was performed with a Bio-Rad C100 Thermal Cycler (Bio-Rad Laboratories, Hercules, CA). The cDNAs were diluted 1 : 20 with the reaction mixture from the Ex Taq PCR kit (Takara), and the PCR was performed by standard 3 step amplification protocol consisting of hot start enzyme activation at 95°C for 10 minutes followed by 35 cycles of amplification at 95°C for 30 seconds, 60°C for 60 seconds, and 72°C for 60 seconds. For real-time PCR, which was performed with a Takara Thermal Cycler Dice Real Time System TP800 (Takara), the cDNAs were diluted 1 : 25 in the reaction mixture containing SYBR Premix EX Taq II (Takara). The real-time PCR program consisted of hot start enzyme activation at 95°C for 10 seconds followed by 45 cycles of amplification at 95°C for 10 seconds and 60°C for 40 seconds. Finally, to obtain a dissociation curve, a final cycle was performed at 95°C for 1 minute, 60°C for 30 seconds, and 95°C for 10 seconds. For data analysis, the mouse or human *glyceraldehyde-3-phosphate dehydrogenase* (*Gapdh* or *GAPDH*) housekeeping gene was used as an internal control. Induction values were calculated using analysis software (Takara). Primer sequences are available upon request from the TAKARA BIO INC. website (http://www.takara-bio.co.jp/).

MiRNA array. The miRNA expression profile was obtained by using a Mouse miRNA microarray 8 × 15 K (Agilent Technologies, Santa Clara, CA) according to the manufacturer's protocol. Total RNA was prepared from fractionated E-EVs using the miRNA easy Mini Kit (Qiagen). RNA quality was measured with an Agilent 2100 Bioanalyzer (Agilent Technologies). Synthesis of probes, and hybridization to the Mouse miRNA microarray 8 × 15 K were performed by using the miRNA Complete Labeling and Hyb Kit (Agilent Technologies). Hybridized samples were analyzed using a Microarray Scanner (G2505B, Agilent Technologies) and GeneSpring GX software (Agilent Technologies) according to standard protocols. The miRNA array data were analyzed using Ingenuity Pathway Analysis (Ingenuity Systems, http://www.ingenuity.com/).

Western blotting. For E-EV marker analyses, E-EVs that were fractionated from the culture media of b.End5 cells after CytoCombo + LPS stimulation were used as sample. For the control, b.End5 cells were used. For VEGF-B analyses, E-EVs that were fractionated from the culture media of b.End5 cells after CytoCombo stimulation were added (100 μg) to HBPCs cultured in a collagen type I-coated 24-well plate (BD Bioscience), and the plate was incubated at 37°C for 48 hours. Sample preparations and all other procedures for western blotting have been described elsewhere[64]. Briefly, cells were lysed using RIPA buffer (Thermo Fisher, Waltham, MA) on ice. Whole cell lysates were separated by SDS-PAGE and then electrophoretically transferred to polyvinylidene difluoride membranes. The membranes were incubated for 1 hour at room temperature in a 50 mM Tris buffer containing 150 mM NaCl, 0.05% Tween 20, and 5% BSA for blocking. The membranes were then probed with rabbit anti-VEGFR-2 (1 : 500; Cell Signaling Technology), rabbit anti-CD62E (1 : 100; Abcam), rabbit anti-VEGF-B (1 : 100; Abcam), and mouse anti-GAPDH (1 : 5,000; Merck Millipore, Billerica, MA) antibodies. The membranes were washed in a 50 mM Tris buffer containing 150 mM NaCl, and 0.05% Tween 20, and were incubated with the appropriate horseradish peroxidase-conjugated secondary antibodies. Immunoreactive bands were detected using enhanced chemiluminescence reagents (GE Healthcare Bio-Sciences AB, Uppsala, Sweden) according to the manufacturer's instructions.

Statistical analysis. Statistical significance was determined using Student's t-test, or one- or two-way analysis of variance (ANOVA) with Tukey's or Newman-Keuls multiple comparisons as a post hoc analysis for ANOVA. P values less than 0.05 were considered statistically significant. Graphs were drawn using GraphPad Prism 6 (GraphPad Software, Inc., La Jolla, CA). Quantified data are presented as mean ± SEM.

1. Raposo, G. & Stoorvogel, W. Extracellular vesicles: exosomes, microvesicles, and friends. *J Cell Biol* **200**, 373–383 (2013).
2. Gould, S. J. & Raposo, G. As we wait: coping with an imperfect nomenclature for extracellular vesicles. *J Extracell Vesicles* **2**, 20389 (2013).
3. Kosaka, N., Iguchi, H. & Ochiya, T. Circulating microRNA in body fluid: a new potential biomarker for cancer diagnosis and prognosis. *Cancer Sci* **101**, 2087–2092 (2010).
4. Beyer, C. & Pisetsky, D. S. The role of microparticles in the pathogenesis of rheumatic diseases. *Nat Rev Rheumatol* **6**, 21–29 (2010).
5. Antonyak, M. A. *et al.* Cancer cell-derived microvesicles induce transformation by transferring tissue transglutaminase and fibronectin to recipient cells. *Proc Natl Acad Sci U S A* **108**, 4852–4857 (2011).
6. Ratajczak, J., Wysoczynski, M., Hayek, F., Janowska-Wieczorek, A. & Ratajczak, M. Z. Membrane-derived microvesicles: important and underappreciated mediators of cell-to-cell communication. *Leukemia* **20**, 1487–1495 (2006).
7. Kawamoto, T. *et al.* Tumor-derived microvesicles induce proangiogenic phenotype in endothelial cells via endocytosis. *PLoS One* **7**, e34045 (2012).
8. Thery, C. Exosomes: secreted vesicles and intercellular communications. *F1000 Biol Rep* **3**, 15 (2011).
9. Mostefai, H. A. *et al.* Circulating microparticles from patients with septic shock exert protective role in vascular function. *Am J Respir Crit Care Med* **178**, 1148–1155 (2008).
10. Simak, J., Gelderman, M. P., Yu, H., Wright, V. & Baird, A. E. Circulating endothelial microparticles in acute ischemic stroke: a link to severity, lesion volume and outcome. *J Thromb Haemost* **4**, 1296–1302 (2006).
11. Petrozella, L. *et al.* Endothelial microparticles and the antiangiogenic state in preeclampsia and the postpartum period. *Am J Obstet Gynecol* **207**, 140 e120–146 (2012).
12. Boulanger, C. M., Amabile, N. & Tedgui, A. Circulating microparticles: a potential prognostic marker for atherosclerotic vascular disease. *Hypertension* **48**, 180–186 (2006).
13. Koga, H. *et al.* Elevated levels of VE-cadherin-positive endothelial microparticles in patients with type 2 diabetes mellitus and coronary artery disease. *J Am Coll Cardiol* **45**, 1622–1630 (2005).
14. Agouni, A. *et al.* Endothelial dysfunction caused by circulating microparticles from patients with metabolic syndrome. *Am J Pathol* **173**, 1210–1219 (2008).
15. Martínez, M. C., Tesse, A., Zobairi, F. & Andriantsitohaina, R. Shed membrane microparticles from circulating and vascular cells in regulating vascular function. *Am J Physiol Heart Circ Physiol* **288**, H1004–1009 (2005).
16. Bartel, D. P. MicroRNAs: genomics, biogenesis, mechanism, and function. *Cell* **116**, 281–297 (2004).
17. Bartel, D. P. MicroRNAs: target recognition and regulatory functions. *Cell* **136**, 215–233 (2009).
18. Montgomery, R. L. & van Rooij, E. MicroRNA regulation as a therapeutic strategy for cardiovascular disease. *Curr Drug Targets* **11**, 936–942 (2010).
19. Small, E. M. & Olson, E. N. Pervasive roles of microRNAs in cardiovascular biology. *Nature* **469**, 336–342 (2011).
20. Hassan, F. *et al.* MiR-101 and miR-144 regulate the expression of the CFTR chloride channel in the lung. *PLoS One* **7**, e50837 (2012).
21. Lee, K. S. *et al.* Functional role of NF-kappaB in expression of human endothelial nitric oxide synthase. *Biochem Biophys Res Commun* **448**, 101–107 (2014).
22. Armulik, A., Genove, G. & Betsholtz, C. Pericytes: developmental, physiological, and pathological perspectives, problems, and promises. *Dev Cell* **21**, 193–215 (2011).
23. Armulik, A. *et al.* Pericytes regulate the blood-brain barrier. *Nature* **468**, 557–561 (2010).
24. Daneman, R., Zhou, L., Kebede, A. A. & Barres, B. A. Pericytes are required for blood-brain barrier integrity during embryogenesis. *Nature* **468**, 562–566 (2010).
25. Bell, R. D. *et al.* Pericytes control key neurovascular functions and neuronal phenotype in the adult brain and during brain aging. *Neuron* **68**, 409–427 (2010).
26. Winkler, E. A., Bell, R. D. & Zlokovic, B. V. Central nervous system pericytes in health and disease. *Nat Neurosci* **14**, 1398–1405 (2011).
27. Rincon, M. Interleukin-6: from an inflammatory marker to a target for inflammatory diseases. *Trends Immunol* **33**, 571–577 (2012).
28. Hua, S. Targeting sites of inflammation: intercellular adhesion molecule-1 as a target for novel inflammatory therapies. *Front Pharmacol* **4**, 127 (2013).
29. Sprague, A. H. & Khalil, R. A. Inflammatory cytokines in vascular dysfunction and vascular disease. *Biochem Pharmacol* **78**, 539–552 (2009).
30. Bannerman, D. D. & Goldblum, S. E. Mechanisms of bacterial lipopolysaccharide-induced endothelial apoptosis. *Am J Physiol Lung Cell Mol Physiol* **284**, L899–914 (2003).
31. Dignat-George, F. & Boulanger, C. M. The many faces of endothelial microparticles. *Arterioscler Thromb Vasc Biol* **31**, 27–33 (2011).
32. Shai, E. & Varon, D. Development, cell differentiation, angiogenesis—microparticles and their roles in angiogenesis. *Arterioscler Thromb Vasc Biol* **31**, 10–14 (2011).
33. Fujita, Y., Kuwano, K., Ochiya, T. & Takeshita, F. The impact of extracellular vesicle-encapsulated circulating microRNAs in lung cancer research. *Biomed Res Int* **2014**, 486413 (2014).
34. Albanese, J. & Dainiak, N. Modulation of intercellular communication mediated at the cell surface and on extracellular, plasma membrane-derived vesicles by ionizing radiation. *Exp Hematol* **31**, 455–464 (2003).
35. Delabranche, X., Berger, A., Boisrame-Helms, J. & Meziani, F. Microparticles and infectious diseases. *Med Mal Infect* **42**, 335–343 (2012).
36. Armulik, A., Abramsson, A. & Betsholtz, C. Endothelial/pericyte interactions. *Circ Res* **97**, 512–523 (2005).
37. Darland, D. C. *et al.* Pericyte production of cell-associated VEGF is differentiation-dependent and is associated with endothelial survival. *Dev Biol* **264**, 275–288 (2003).

38. Yonekura, H. *et al.* Placenta growth factor and vascular endothelial growth factor B and C expression in microvascular endothelial cells and pericytes. Implication in autocrine and paracrine regulation of angiogenesis. *J Biol Chem* **274**, 35172–35178 (1999).
39. de Nigris, F. *et al.* CXCR4/YY1 inhibition impairs VEGF network and angiogenesis during malignancy. *Proc Natl Acad Sci U S A* **107**, 14484–14489 (2010).
40. Barteneva, N. S., Maltsev, N. & Vorobjev, I. A. Microvesicles and intercellular communication in the context of parasitism. *Front Cell Infect Microbiol* **3**, 49 (2013).
41. Sahoo, S. & Losordo, D. W. Exosomes and cardiac repair after myocardial infarction. *Circ Res* **114**, 333–344 (2014).
42. Valadi, H. *et al.* Exosome-mediated transfer of mRNAs and microRNAs is a novel mechanism of genetic exchange between cells. *Nat Cell Biol* **9**, 654–659 (2007).
43. Skog, J. *et al.* Glioblastoma microvesicles transport RNA and proteins that promote tumour growth and provide diagnostic biomarkers. *Nat Cell Biol* **10**, 1470–1476 (2008).
44. Iglesias, D. M. *et al.* Stem cell microvesicles transfer cystinosin to human cystinotic cells and reduce cystine accumulation in vitro. *PLoS One* **7**, e42840 (2012).
45. Curtis, A. M. *et al.* p38 mitogen-activated protein kinase targets the production of proinflammatory endothelial microparticles. *J Thromb Haemost* **7**, 701–709 (2009).
46. Chen, T., Guo, J., Yang, M., Zhu, X. & Cao, X. Chemokine-containing exosomes are released from heat-stressed tumor cells via lipid raft-dependent pathway and act as efficient tumor vaccine. *J Immunol* **186**, 2219–2228 (2011).
47. Tetta, C., Bruno, S., Fonsato, V., Deregibus, M. C. & Camussi, G. The role of microvesicles in tissue repair. *Organogenesis* **7**, 105–115 (2011).
48. Ratajczak, J. *et al.* Embryonic stem cell-derived microvesicles reprogram hematopoietic progenitors: evidence for horizontal transfer of mRNA and protein delivery. *Leukemia* **20**, 847–856 (2006).
49. Thery, C., Amigorena, S., Raposo, G. & Clayton, A. Isolation and characterization of exosomes from cell culture supernatants and biological fluids. *Curr Protoc Cell Biol* **Chapter 3**, Unit 3 22 (2006).
50. Ronquist, G. K., Larsson, A., Stavreus-Evers, A. & Ronquist, G. Prostasomes are heterogeneous regarding size and appearance but affiliated to one DNA-containing exosome family. *Prostate* **72**, 1736–1745 (2012).
51. Guescini, M., Genedani, S., Stocchi, V. & Agnati, L. F. Astrocytes and Glioblastoma cells release exosomes carrying mtDNA. *J Neural Transm* **117**, 1–4 (2010).
52. Balaj, L. *et al.* Tumour microvesicles contain retrotransposon elements and amplified oncogene sequences. *Nat Commun* **2**, 180 (2011).
53. Rak, J. & Guha, A. Extracellular vesicles--vehicles that spread cancer genes. *Bioessays* **34**, 489–497 (2012).
54. Waldenstrom, A., Genneback, N., Hellman, U. & Ronquist, G. Cardiomyocyte microvesicles contain DNA/RNA and convey biological messages to target cells. *PLoS One* **7**, e34653 (2012).
55. Peinado, H. *et al.* Melanoma exosomes educate bone marrow progenitor cells toward a pro-metastatic phenotype through MET. *Nat Med* **18**, 883–891 (2012).
56. Al-Nedawi, K., Meehan, B., Kerbel, R. S., Allison, A. C. & Rak, J. Endothelial expression of autocrine VEGF upon the uptake of tumor-derived microvesicles containing oncogenic EGFR. *Proc Natl Acad Sci U S A* **106**, 3794–3799 (2009).
57. Aliotta, J. M. *et al.* Microvesicle entry into marrow cells mediates tissue-specific changes in mRNA by direct delivery of mRNA and induction of transcription. *Exp Hematol* **38**, 233–245 (2010).
58. Takahashi, H. & Shibuya, M. The vascular endothelial growth factor (VEGF)/VEGF receptor system and its role under physiological and pathological conditions. *Clin Sci (Lond)* **109**, 227–241 (2005).
59. Cao, Y. Positive and negative modulation of angiogenesis by VEGFR1 ligands. *Sci Signal* **2**, re1 (2009).
60. Zhang, F. *et al.* VEGF-B is dispensable for blood vessel growth but critical for their survival, and VEGF-B targeting inhibits pathological angiogenesis. *Proc Natl Acad Sci U S A* **106**, 6152–6157 (2009).
61. Boscolo, E., Mulliken, J. B. & Bischoff, J. VEGFR-1 mediates endothelial differentiation and formation of blood vessels in a murine model of infantile hemangioma. *Am J Pathol* **179**, 2266–2277 (2011).
62. Muramatsu, M., Yamamoto, S., Osawa, T. & Shibuya, M. Vascular endothelial growth factor receptor-1 signaling promotes mobilization of macrophage lineage cells from bone marrow and stimulates solid tumor growth. *Cancer Res* **70**, 8211–8221 (2010).
63. Cao, R. *et al.* VEGFR1-mediated pericyte ablation links VEGF and PlGF to cancer-associated retinopathy. *Proc Natl Acad Sci U S A* **107**, 856–861 (2010).
64. Yamamoto, S. *et al.* Essential role of Shp2-binding sites on FRS2alpha for corticogenesis and for FGF2-dependent proliferation of neural progenitor cells. *Proc Natl Acad Sci U S A* **102**, 15983–15988 (2005).

Acknowledgments

We thank the members of the Department of Pathology at the University of Toyama for helpful discussions. We also thank M. Satake, A. Watanabe, D. Inoue, M. Dohmoto for technical assistance and discussions, and N. Yamamoto, A. Yamamoto, R. Yamamoto for broad-based support. This work was supported by a Grant-in-Aid for Scientific Research (21590589 and 24659112; to S.Y.) from The Ministry of Education, Culture, Sports, Science, and Technology and by The Research Funding for Longevity Sciences (23-9; to S.N.) from the National Center for Geriatrics and Gerontology, and The Advanced Research for Products Mining Programme (10–43; to S.N.) from the National Institute of Biomedical Innovation.

Author contributions

S.Y. and S.N. conceived and designed the project. S.Y., E.A., T.Y., M.M., T.-T.H., H.S., S.H., M.I., Y.N., K.M. and H.M. performed experiments. S.Y. wrote the manuscript with significant input from K.T., T.H., Y.I., H.M., N.M., S.N. and M.S. All authors reviewed the manuscript.

Additional information

Supplementary information accompanies this paper at http://www.nature.com/scientificreports

Competing financial interests: The authors declare no competing financial interests.

How to cite this article: Yamamoto, S. *et al.* Inflammation-induced endothelial cell-derived extracellular vesicles modulate the cellular status of pericytes. *Sci. Rep.* **5**, 8505; DOI:10.1038/srep08505 (2015).

The American Journal of Pathology, Vol. 185, No. 1, January 2015

ELSEVIER

The American Journal of
PATHOLOGY

ajp.amjpathol.org

IMMUNOPATHOLOGY AND INFECTIOUS DISEASES

In Vivo Depletion of CD206$^+$ M2 Macrophages Exaggerates Lung Injury in Endotoxemic Mice

Kenta Kambara,*† Wakana Ohashi,* Kengo Tomita,* Michinori Takashina,* Shiho Fujisaka,† Ryuji Hayashi,† Hisashi Mori,‡ Kazuyuki Tobe,† and Yuichi Hattori*

From the Departments of Molecular and Medical Pharmacology and Neuroscience‡ and the First Department of Internal Medicine,† Graduate School of Medicine and Pharmaceutical Sciences, University of Toyama, Toyama, Japan*

Accepted for publication September 17, 2014.

Address correspondence to Yuichi Hattori, M.D., Ph.D., Department of Molecular and Medical Pharmacology, Graduate School of Medicine and Pharmaceutical Sciences, University of Toyama, Toyama 930-0194, Japan. E-mail: yhattori@med.u-toyama.ac.jp.

Although phenotypically polarized macrophages are now generally classified into two major subtypes termed proinflammatory M1 and anti-inflammatory M2 macrophages, a contributory role of lung M2 macrophages in the pathophysiological features of acute lung injury is not fully understood. Herein, we show in an endotoxemic murine model that M2 macrophages serve as key anti-inflammatory cells that play a regulatory role in the severity of lung injury. To study whether M2 macrophages can modify inflammation, we depleted M2 macrophages from lungs of CD206-diphtheria toxin (DT) receptor transgenic (Tg) mice during challenge with lipopolysaccharide. The i.p. administration of DT depleted CD206-positive cells in bronchoalveolar lavage fluid. The use of M2 macrophage markers Ym1 and arginase-1 identified pulmonary CD206-positive cells as M2 macrophages. A striking increase in neutrophils in bronchoalveolar lavage fluid cell contents was found in DT-treated CD206-DT receptor Tg mice. In CD206-DT receptor Tg mice given DT, endotoxin challenge exaggerated lung inflammation, including up-regulation of proinflammatory cytokines and increased histological lung damage, but the endotoxemia-induced increase in NF-κB activity was significantly reduced, suggesting that M2 phenotype-dependent counteraction of inflammatory insult cannot be attributed to the inhibition of the NF-κB pathway. Our results indicate a critical role of CD206-positive pulmonary macrophages in triggering inflammatory cascade during endotoxemic lung inflammation. *(Am J Pathol 2015, 185: 162–171; http://dx.doi.org/10.1016/j.ajpath.2014.09.005)*

Macrophages are critical regulators of many organ systems, including innate and adaptive immunity, systemic metabolism, hematopoiesis, vasculogenesis, malignancy, and reproduction.[1] Macrophages differentiate into functionally distinct immunological populations depending on the microenvironments. On the basis of type 1/2 helper T-cell polarization concepts,[2] phenotypically polarized macrophages are now generally termed proinflammatory M1 and anti-inflammatory M2.[3,4] Macrophages exposed to microbial products and interferon-γ become classically activated macrophages (M1), which produce copious amounts of proinflammatory cytokines and chemokines; key among these are tumor necrosis factor (TNF)-α, IL-1β, IL-6, IL-12, and chemokine ligand 2. The same macrophages also produce reactive oxygen intermediates, and function predominantly in inflammation, tissue damage, killing of intracellular microbes, and increased tumoricidal activity.[3] Recent studies also suggest that the phenotypic switching of adipose tissue macrophages from M2 to M1 is generated by obesity, leading to systemic inflammation and insulin resistance.[5–7] In contrast, alternative activation of macrophages is promoted by a variety of stimuli, such as IL-4, IL-10, IL-13, and glucocorticoids, that elicit different M2 forms. M2 macrophages up-regulate scavenger, mannose receptor, galactose receptor, and IL-1 receptor antagonist, and down-regulate IL-1β and other proinflammatory cytokines.[3,8,9] They are principally able to tune inflammatory responses and adaptive type 2 helper T-cell immunity, and to promote tissue remodeling, angiogenesis, and tumor development.[3,10] Furthermore, M2

Supported by the Ministry of Education, Culture, Sports, Science and Technology of Japan Grants-in-Aid for Scientific Research 18209033 and 21591126 (K.T.).

Disclosures: None declared.

http://dx.doi.org/10.1016/j.ajpath.2014.09.005

macrophage activation can protect neurons and facilitate neuronal regeneration in Alzheimer disease.[11] M2-polarized macrophages are further subdivided into the wound-healing M2a (elicited by IL-4 and IL-13), the regulatory M2b (after stimulation by immune complexes in the presence of Toll-like receptor ligands), and the M2c (when exposed to anti-inflammatory stimuli, such as glucocorticoids, IL-10, and transforming growth factor-β),[4] but this sub-classification may not fully represent the complexity of the transitional states of macrophage activation, which is finely tuned in response to different microenvironments.[12]

Acute lung injury (ALI) is a common and highly morbid clinical disease marked by respiratory failure attributable to increased pulmonary endothelial and epithelial permeability, leading to alveolar flooding, and neutrophil accumulation in alveolar spaces and in adjacent capillaries.[13,14] Although neutrophil influx and activation within the lung play a crucial role in the pathogenesis of ALI,[15] growing evidence indicates that macrophages also contribute to the modulation of lung inflammation and the resultant lung injury.[16–18] Several studies have found that macrophage depletion with clodronate-lisosomes results in attenuation of lung injury after endotoxin administration, ischemia-reperfusion, and mechanical ventilation.[19–22] Conversely, other studies suggest that the recruitment of macrophages to the lung is associated with attenuated lung injury.[23,24] One possible explanation for such disparate roles of macrophages in ALI may be related to different depletion or recruitment of heterogeneous populations of proinflammatory and anti-inflammatory macrophages in the lung. However, how M2 macrophages have a protective anti-inflammatory role under the pathological condition of ALI is not fully understood.

Herein, we decided to deplete M2 macrophages in mice during exposure to lipopolysaccharide (LPS). We generated a line of transgenic (Tg) mice expressing human diphtheria toxin (DT) receptor under the control of the *Mrc1* gene promoter. Murine cells are naturally resistant to DT because they lack functional cell surface receptors for the toxin.[25–27] Thus, the technique with human DT receptor transduction allows us to achieve efficient inducible ablation of a specific type of murine cells by DT administration *in vivo*. Because Mrc1 (alias CD206) is a cell surface receptor as an M2 phenotypic marker, systemic administration of DT was able to lead to a sharp decline in lung M2 macrophages in CD206-DT receptor Tg mice. Herein, we identify lung M2 macrophages as key anti-inflammatory cells that play a regulatory role in the severity of endotoxin-induced lung injury.

Materials and Methods

Generation and Screening of CD206-DT Receptor Tg Mice

We obtained the mouse BAC clone RP 24-377 D19 carrying a 152-kbp insert containing the exon coding translational start Met and upstream 133-kbp sequence of *CD206* gene from the BACPAC Resources Center CHORI (Oakland, CA). The plasmid pTRECK6 that includes noncoding exon and intron from rabbit β-globulin gene, human HB-EGF (DT receptor) cDNA, and rabbit β-globulin and simian virus 40 polyadenylation (pA) signals was kindly provided by Dr. Kenji Kohno (Nara Institute of Science and Technology, Nara, Japan).[28,29] By using a Counterselection BAC modification kit (Gene Bridges, Dresden, Germany), we inserted the noncoding exon and intron from rabbit β-globulin gene, human DT receptor cDNA, and rabbit β-globulin and simian virus 40 pA signals at the initiation site of translation in the *CD206* gene to yield the pTg-CD206-DT receptor (Figure 1A).

The purified pTg-CD206-DT receptor BAC DNA was microinjected into pronuclei of fertilized one-cell embryos from C57BL/6 mice. Founder mice were crossed with C57BL/6 mice to produce +/CD206$^{DT\ receptor}$ mice. The wild-type (WT; +/+) and heterozygous CD206-DT receptor (+/CD206DTR) littermates were used for analysis. All mice were housed in a specific pathogen-free facility. Experiments were performed according to institutional guidelines.

For the genotyping of the Tg mouse lines by Southern blot analysis, genomic DNA prepared from tail biopsy specimens was digested with BamHI, separated by electrophoresis on a 0.6% agarose gel, and transferred to a nylon membrane (Hybond-N$^+$; GE Healthcare Japan, Tokyo, Japan). Hybridization was conducted with a 900-bp ^{32}P-labeled DNA fragment derived from the exon 1 and intron 1 (Figure 1B). The detected band sizes of endogenous and Tg genes were 8.3 and 3.8 kb, respectively.

Experimental Procedures

In a first series of experiments to examine the effects of M2 macrophage depletion under normal noninflammatory conditions, CD206-DT receptor Tg mice and WT littermates received an i.p. injection of 15 μg/kg DT. Mice were administered DT for 3 consecutive days and sacrificed 24 hours after the last injection (Figure 2A). Blood samples were collected, and various tissues and organs were removed. Some mice were given phosphate-buffered saline (PBS) instead of DT.

In another series of experiments to address the role of M2 macrophages in endotoxin-induced ALI, mice received an i.p. injection of 15 μg/kg DT for 3 consecutive days and were subsequently challenged with i.v. LPS (0.1 mg/kg; List Biological Laboratories, Campbell, CA) 24 hours after the last injection. Mice were sacrificed 2 hours later, and blood collection and lung tissue isolation were performed (Figure 3A).

RNA Extraction and Quantitative Real-Time PCR

Total RNA was isolated from tissues with an RNeasy Mini Kit (Qiagen, Tokyo, Japan). RNA was reverse transcribed to cDNA, and real-time PCR analyses were performed as

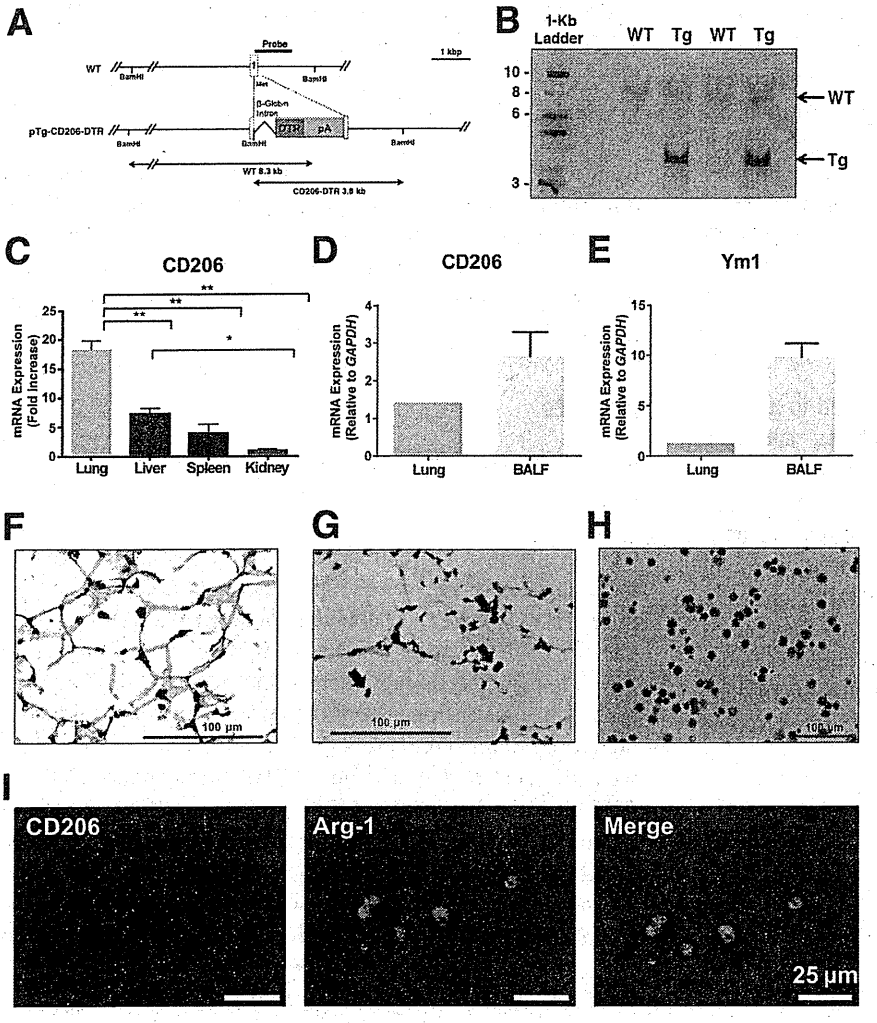

Figure 1 CD206 expression in C57BL/6 mice. **A:** Schematic representation of WT and DT receptor (DTR)—inserted transgene in BAC DNA (pTg-CD206-DT receptor). Exons 1 through 3 of *CD206* gene are indicated by an open box. Met is the initiation site of translation in *CD206*. In the pTg-CD206-DT receptor BAC DNA, rabbit β-globin intron, human DT receptor cDNA, and rabbit β-globin/simian virus 40 pA signals are indicated by line and gray box. The probe used for Southern blot analysis is indicated as a solid line together with the predicted hybridizing fragments. After insertion of DT receptor, the CD206 of the transgene is not expressed. **B:** Southern blot analysis of BamHI-digested genomic DNA from CD206-DT receptor Tg mice. Genomic DNAs were hybridized with the CD206 probe, as shown in **A**. Location of WT (8.6 kbp) and CD206-transgene (Tg; 3.8 kbp)-derived bands are shown. The positions of DNA size markers (kbp) are indicated on the left. **C:** CD206 mRNA expression in different tissues of normal mice. The data are expressed as a fold increase above kidney value normalized to 18S (n = 3 mice). CD206 (**D**) and Ym1 (**E**) mRNA expression in lung tissues and in BALF from normal mice. The data are normalized to GAPDH (n = 3). The IHC detection of arginase-1—positive cells (**F**) and CD206-positive cells (**G**) in lung sections and in BALF (**H**) from normal mice. Lung sections and BALF were stained with hematoxylin. **Arrows** indicate CD206-positive cells (**G**). **I:** Immunofluorescence images in BALF. **Left panel:** CD206 (red). **Middle panel:** arginase-1 (Arg-1; green). **Right panel:** Overlap images with the two stains are presented. Nuclei were counterstained with DAPI (blue). Shown are representative micrographs from two independent experiments. $^{*}P < 0.05$, $^{**}P < 0.01$.

described previously[30] using a Takara RNA PCR kit (Takara Bio, Ohtsu, Japan). Thermal cycler parameters were as follows: 1 cycle of 50°C for 2 minutes, 50 cycles of denaturation (95°C for 15 seconds), and combined annealing/extension (60°C for 30 seconds). Gene expression changes were calculated by the comparative C_T method, and 18S ribosomal RNA was used as the reference gene for normalization.

Enzyme Immunoassay for Cytokines

Blood levels of IL-1β, TNF-α, monocyte chemotactic protein (MCP)-1, and IL-6 were measured by the use of a commercially available enzyme-linked immunosorbent assay (ELISA) kit (R&D Systems, Minneapolis, MN), according to the manufacturer's instructions. The plate was read on a microplate reader (Nippon-InterMed, Tokyo, Japan). Assays were performed in duplicate.

Histological Examination

For routine histological examination, inflation-fixed lungs were harvested, fixed, dehydrated, paraffin embedded, and sliced into sections (4 μm thick).[30,31] After deparaffinization, slides were stained with hematoxylin and eosin (H&E) using standard methods. A semiquantitative morphometric analysis of lung injury was performed by scoring from 0 to 4: 0 indicates none; 1 indicates light; 2 indicates moderate; 3 indicates severe; and 4 indicates very severe. The scores are for the following categories: neutrophil infiltration, pulmonary edema, and disorganization of lung parenchyma and hemorrhage.[30] A total lung injury score was calculated by adding the individual scores in every animal and averaging the total values in each group. All of the histological studies were performed in a blinded manner (K.K.).

IHC Data

Frozen lung sections (5 mm thick) were fixed in acetone for 10 minutes at −20°C and air dried. Bronchoalveolar lavage (BAL) was performed with five aliquots of 5 mL of PBS instilled into the lungs and gently withdrawn. Cells obtained from the total BAL fluid (BALF) were spun at 113 × g for 10 minutes onto glass slides by use of a Cytospin 4 (Thermo Fisher Scientific, Yokohama, Japan). Then, they were fixed with 4% buffered formalin solution for 10 minutes at room temperature.

Endogenous peroxidase activity was quenched by incubation in 0.3% hydrogen peroxide for 15 minutes. After incubation overnight at 4°C with anti-CD206 antibody (AbD Serotec, Raleigh, NC) or anti—arginase-1 antibody (Sigma-Aldrich, St. Louis, MO), the samples were exposed to anti-rat or anti-rabbit IgG conjugated with horseradish peroxidase. Bound antibody was visualized by a light microscopy with diaminobenzidine. Omission of primary antibody and staining with nonimmune IgG served as negative control.

Immunofluorescence Staining

Cells obtained from the total BALF were adhered to a glass-bottom dish, fixed with 4% paraformaldehyde, and permeabilized in Perm Buffer (BD Biosciences, San Diego, CA). Cells were exposed to the fluorescent antibody Alexa 546—conjugated anti-rat IgG and Alexa 488—conjugated anti-rabbit IgG (Life Technologies, Carlsbad, CA) after overnight incubation with the primary antibody, anti-CD206 antibody and anti—arginase-1 antibody. The nucleus was counterstained with DAPI. Immunofluorescence images were observed under an Olympus (Tokyo, Japan) BX-51 fluorescence microscope and processed using Adobe Photoshop CS3 software (Adobe, San Jose, CA).

Cell Counting in BALF

The alterations in cells in BALF were examined as described previously.[31] Cells in BALF obtained as mentioned above were counted with a hemacytometer. Slides were stained with Wright stain, and cell differentiation was tabulated using light microscopy.

NF-κB and AP-1 Binding Assays

Nuclear protein extracts from freshly isolated lungs were obtained with a commercially available nuclear extraction kit (Sigma-Aldrich), as described in the manufacturer's manual. TransAM NF-κB and TransAM AP-1 kits (Active Motif, Carlsbad, CA) were used to quantify the binding of p65 to the NF-κB site and c-Jun and c-Fos to the activator protein (AP)-1 site, according to the manufacturer's instructions. TransAM kits are DNA-binding ELISAs that quantify transcription factor activation in tissues.

Electrophoretic Mobility Shift Assay

NF-κB and AP-1 DNA binding reactions were performed according to the manufacturer's protocol using the Odyssey Infrared electrophoretic mobility shift assay kit (Li-Cor Biosciences, Lincoln, NE) and nuclei extracts from lung tissues. Double-stranded IRDye 700 infrared dye-labeled oligonucleotides with consensus sequences of NF-κB (forward, 5′-AGTTGAGGGGACTTTCCCAGGC-3′ and reverse, 5′-GCCTGGGAAAHTCCCCTCAACT-3′) and AP-1 (forward, 5′-CGCTTGATGACTCAGCCGGAA-3′ and reverse, 5′-TTCCGGCTGAGTCATCAAGCG-3′) were used.

Statistical Analysis

Data were analyzed by the use of Prism software version 6 (GraphPad Software, San Diego, CA). Statistical analysis was performed by Student's unpaired *t*-test or one-way analysis of variance, followed by Tukey's multiple comparison test. Differences were considered significant at $P \leq 0.05$. Data are presented as means ± SEM.

Results

CD206-Positive Cell Expression and Distribution in Mice

CD206 mRNAs were transcribed in a variety of tissues, including lung, liver, spleen, and kidney, of normal C57BL/6 mice, but they were most abundant in lung tissues (Figure 1C). CD206 mRNA expression levels were evidently higher in BALF than in lung tissues when normalized to glyceraldehyde-3-phosphate dehydrogenase (GAPDH) (Figure 1D). Likewise, high levels of mRNA expression of the classic M2 marker Ym1 were detected in BALF (Figure 1E). Immunohistochemical (IHC) studies showed that CD206-positive cells were present in the alveoli (Figure 1G) and constituted a great portion of the whole cells in BALF (Figure 1H). Arginase-1, a marker for the M2 subset, behaved in the same way as CD206 in terms of the alveolar localization (Figure 1F). Moreover, merging of CD206 and arginase-1 showed that CD206-positive cells in BALF were labeled with arginase-1 (Figure 1I).

DT Treatment of CD206-DT Receptor Tg Mice

DT treatment resulted in a sharp reduction in CD206 mRNA levels in lungs of CD206-DT receptor Tg mice without any change in those of WT mice (Figure 2B). Similarly, Ym1 mRNA expression in lungs was reduced when DT was given to CD206-DT receptor Tg mice (Figure 2C). Consistent with the effect on CD206 mRNA in lung tissues, DT treatment caused marked decreases in the CD206 and Ym1 mRNA expression levels (Figure 2, D and E) and the CD206-positive cell number (Figure 2, F and G) in BALF from the CD206-DT receptor Tg animal compared with WT. Furthermore, an immunofluorescence labeling study showed that no cells labeled with CD206 or arginase-1 were detectable in BALF from CD206-DT receptor Tg mice (data not shown).

DT treatment did not substantially affect mRNA levels of proinflammatory cytokines, IL-1β, TNF-α, MCP-1, and IL-6, in lungs of WT mice. On the other hand, CD206-DT receptor Tg mice exhibited up-regulation of these proinflammatory cytokine mRNAs in response to DT treatment (Figure 2H). However, the effects of DT treatment on inflammatory gene expression were much less pronounced when compared with those of further challenge with LPS in

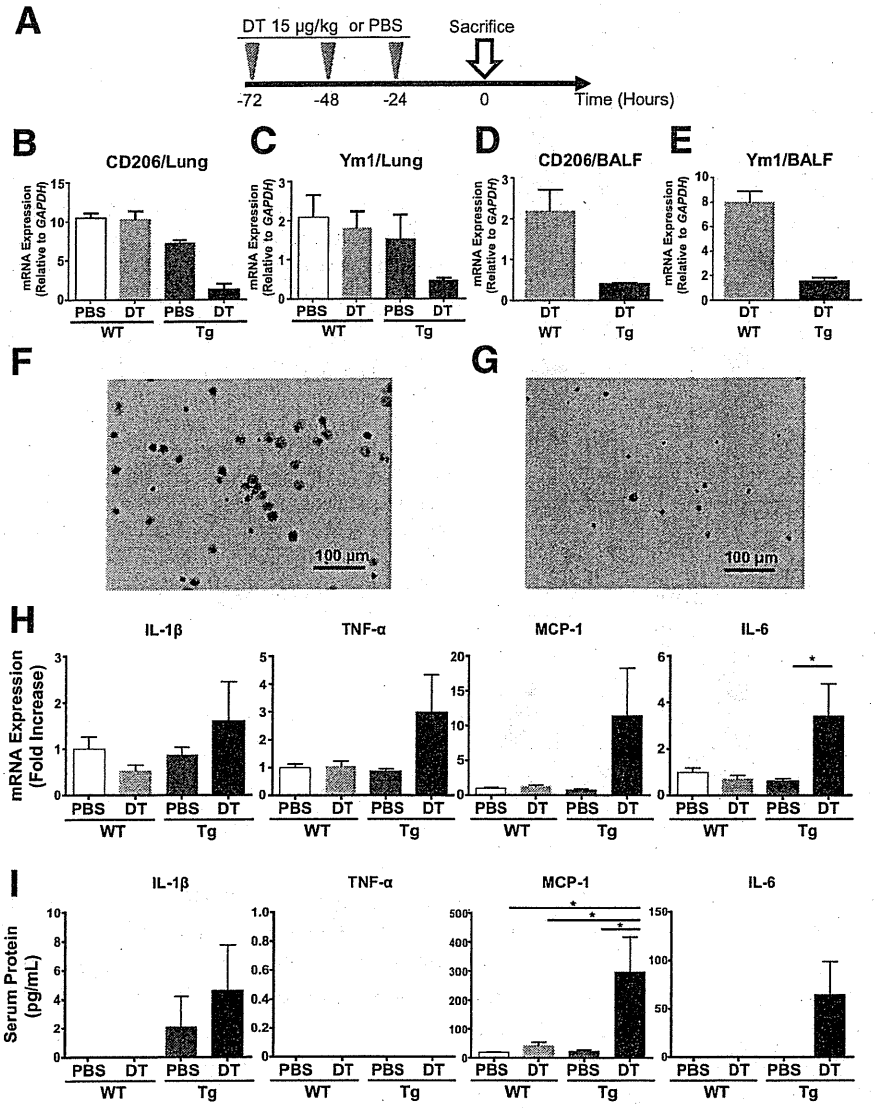

Figure 2 DT treatment on CD206 expression and proinflammatory cytokine production in CD206-DT receptor Tg mice. **A:** Experimental protocol. Mice were administered DT (or PBS) once daily for 3 days. The animals were then sacrificed 24 hours after the last DT injection. **B—E:** CD206 and Ym1 mRNA expression in lung tissues and BALF (n = 2 to 4). The data are normalized to GAPDH mRNA. IHC detection of CD206-positive cells in BALF from WT mice (**F**) and from DT-treated CD206-DT receptor Tg mice (**G**). Shown are representative micrographs from two independent experiments. **H:** mRNA levels of cytokines in lungs. The data are expressed as a fold increase above WT normalized 18S. **I:** Blood levels of cytokines. n = 7 to 8 (**H** and **I**). $^*P < 0.05$.

DT-treated CD206-DT receptor Tg mice (Supplemental Figure S1).

When blood levels of proinflammatory cytokines were measured via an ELISA, the WT animals had low levels of the cytokines examined herein regardless of whether DT was given. In contrast, IL-1β, MCP-1, and IL-6 showed an evident increase in CD206-DT receptor Tg mice when treated with DT, except that TNF-α was undetectable even though DT was administered (Figure 2I).

Effect of LPS in DT-Treated CD206-DT Receptor Tg Mice

DT treatment was without effect on lung and BALF CD206 mRNA levels in WT mice. When a low dose (0.1 mg/kg) of LPS was i.v. injected to DT-treated WT mice, CD206 mRNA levels were substantially unchanged in both lungs and BALF (Figure 3, B and C). Interestingly, challenge with the low dose of LPS did not alter the total number of BALF cells in WT mice (Supplemental Figure S2). This is due to the BALF cells being mainly composed of CD206-positive macrophages. However, a notable increase in neutrophils in BALF cell contents was found in DT-treated CD206-DT receptor Tg mice (Supplemental Figure S2).

LPS challenge led to up-regulation of IL-1β, TNF-α, MCP-1, and IL-6 mRNA levels in lungs of WT mice. This up-regulation was strikingly enhanced in DT-treated CD206-DT receptor Tg mice (Figure 3D). The ability of LPS at 0.1 mg/kg to up-regulate blood levels of TNF-α, MCP-1, and IL-6 was less pronounced in WT mice regardless of treatment with DT, although IL-1β responded relatively well to LPS. However, LPS caused a significant and substantial impact on all proinflammatory cytokines examined herein in DT-treated CD206-DT receptor Tg mice (Figure 3E). LPS also led to an increase in the mRNA level of the anti-inflammatory cytokine IL-10 (Supplemental Figure S3). DT treatment enhanced the LPS-induced increase in IL-10 mRNA in CD206-DT receptor Tg mice.

Histological examination of H&E-stained sections of the lungs revealed that WT mice had alveolar septae that were normal in appearance, with no intra-alveolar inflammation

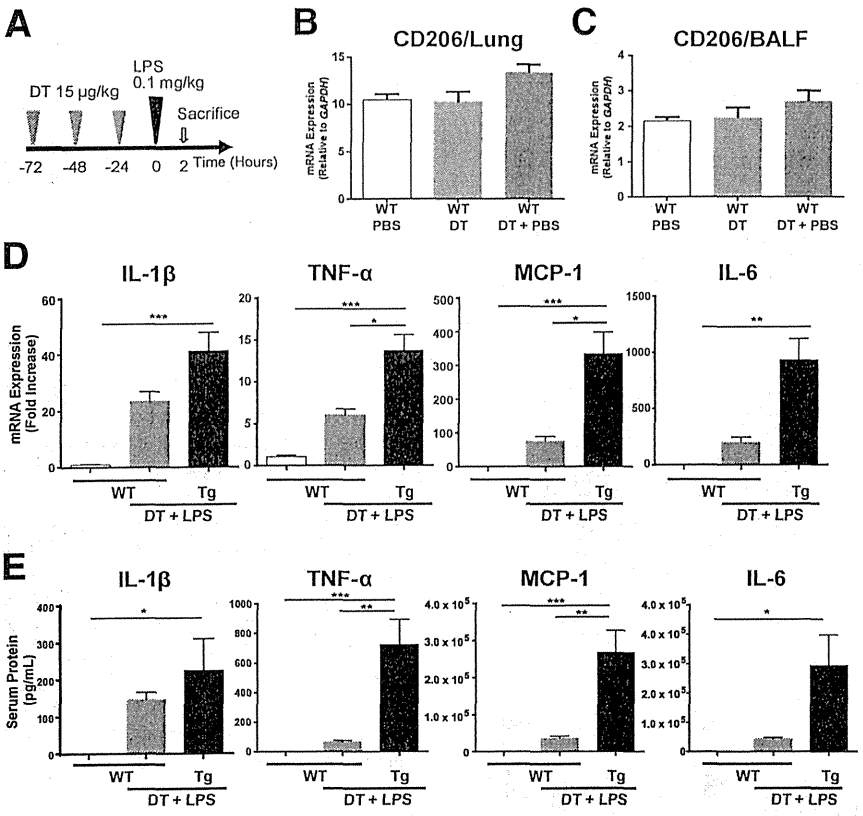

Figure 3 DT treatment on CD206 expression and proinflammatory cytokine production in CD206-DT receptor Tg mice exposed to LPS. **A:** Experimental protocol. Mice were administered DT once daily for 3 days. The animals then received an i.v. injection of LPS 24 hours after the last DT treatment and were sacrificed 2 hours later. CD206 mRNA expression in lung tissues (**B**) and BALF (**C**) from WT mice treated with PBS, DT, or DT plus LPS ($n = 4$). The data are normalized to GAPDH mRNA. **D:** Effect of LPS challenge on mRNA levels of cytokines in lungs. The data are expressed as a fold increase above control WT normalized to 18S. **E:** Effect of LPS challenge on blood levels of cytokines. $n = 5$ to 10 (**D** and **E**). $^{*}P < 0.05$, $^{**}P < 0.01$, and $^{***}P < 0.001$.

(Figure 4A). Lung histopathological analysis of WT mice given LPS showed modest inflammatory cell infiltrate (Figure 4B). DT-treated CD206-DT receptor Tg mice that received LPS had massive cell infiltration, hemorrhage resulting from ruptured capillary vessels, and diffuse septal edema (Figure 4C). Semiquantitative assessment using the lung injury score demonstrated that the score was significantly higher in CD206-DT receptor Tg mice treated with DT than in untreated Tg animals (Figure 4D). When DT-treated CD206-DT receptor Tg mice were challenged with LPS, the score increased strikingly.

To examine the activation of the proinflammatory transcription factor NF-κB in lungs after LPS challenge, NF-κB DNA binding activity in nuclear protein extracts from lungs was quantitatively measured with its ELISA. The DNA binding activity of NF-κB was greatly increased in WT mice after LPS injection. This increase was significantly attenuated in DT-treated CD206-DT receptor Tg mice (Figure 5A). Another proinflammatory transcription factor, AP-1, consists of Jun and Fos family proteins. Thus, c-Jun and c-Fos proto-oncogenes encode proteins that form a complex that regulates transcription from promoters containing AP-1 activation elements.[32] Both c-Jun and c-Fos binding activities were significantly increased when WT mice were challenged with LPS. Further increases in these binding activities in response to LPS were observed in DT-treated CD206-DT receptor Tg mice (Figure 5A). These findings obtained using the ELISA method were confirmed by gel mobility shift assay. The LPS-induced great increase in the NF-κB binding was blunted when DT was given to CD206-DT receptor Tg mice (Figure 5B). In contrast, DT treatment markedly heightened the LPS-induced increase in the AP-1 binding in CD206-DT receptor Tg mice.

Discussion

The concept of macrophages existing in functionally distinct phenotypes from proinflammatory to anti-inflammatory states has been fully established by detailed studies on M1 and M2 macrophages.[3,4,8,9] A growing body of evidence is accumulating that macrophages are key regulators of the induction and resolution phases of ALI, suggesting distinct roles of macrophage subpopulations.[33] Understanding this heterogeneity of pulmonary macrophages may be important in developing strategies to modulate ALI. However, there is no direct evidence that pulmonary M2 macrophages make a significant contribution to the pathophysiological features of ALI. In this work, we addressed this issue by studying how depletion of M2 macrophages can modify lung inflammation in endotoxemic mice.

CD206 encodes the mannose receptor C-type lectin, a cell surface protein that belongs to a family of C-type lectin receptors.[34] This endocytic receptor is known to be expressed on macrophages and probably other types of cells, including airway smooth muscle cells.[35–38] The expression of the